Physics of Fluids

RESEARCH ARTICLE | OCTOBER 28 2014

Two-point statistics for turbulent boundary layers and channels at Reynolds numbers up to $\delta^+ \approx 2000$

Juan A. Sillero ; Javier Jiménez; Robert D. Moser

Check for updates

Physics of Fluids 26, 105109 (2014)
https://doi.org/10.1063/1.4899259

View Online
Export Citation

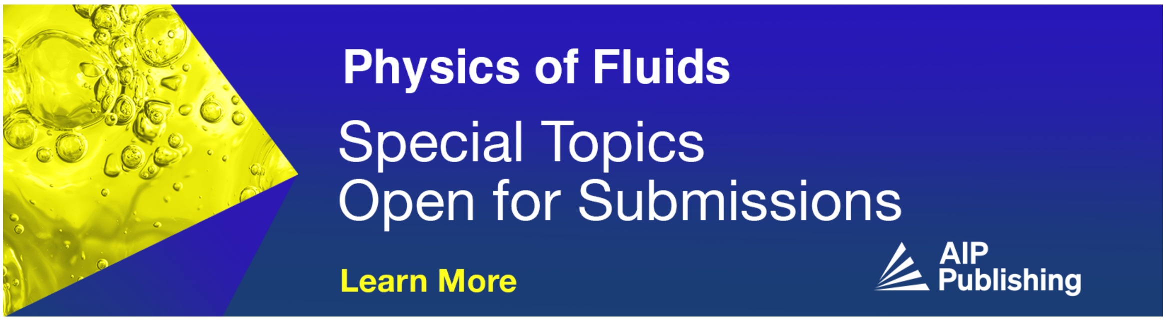

AIP Publishing

PHYSICS OF FLUIDS **26**, 105109 (2014)

Two-point statistics for turbulent boundary layers and channels at Reynolds numbers up to $\delta^+ \approx 2000$

Juan A. Sillero,[1,a)] Javier Jiménez,[1,b)] and Robert D. Moser[2]
[1] *School of Aeronautics, U. Politécnica de Madrid, 28040 Madrid, Spain*
[2] *Department of Mechanical Engineering and Institute for Computational Engineering and Sciences, University of Texas, Austin, Texas 78735, USA*

(Received 4 July 2014; accepted 13 October 2014; published online 28 October 2014)

Two-point statistics are presented for a new direct simulation of the zero-pressure-gradient turbulent boundary layer in the range $Re_\theta = 2780$–6680, and compared with channels in the same range of Reynolds numbers, $\delta^+ \approx 1000$–2000. Three-dimensional spatial correlations are investigated in very long domains to educe the average structure of the velocity and pressure fluctuations. The streamwise velocity component is found to be coherent over longer distances in channels than in boundary layers, especially in the direction of the flow. For weakly correlated structures, the maximum streamwise length is $\mathcal{O}(7\delta)$ for boundary layers and $\mathcal{O}(18\delta)$ for channels, attained at the logarithmic and outer regions, respectively. The corresponding lengths for the spanwise and wall-normal velocities and for the pressure are shorter, $\mathcal{O}(\delta$-$2\delta)$. The correlations are shown to be inclined to the wall at angles that depend on the distance from the wall, on the variable being considered, and on the correlation level used to define them. All these features change little between the two types of flows. Most the above features are also approximately independent of the Reynolds number, except for the pressure, and for the streamwise velocity structures in the channel. Further insight into the flow is provided by correlations conditioned on the intensity of the perturbations at the reference point, or on their sign. The statistics of the new simulation are available in our website. © *2014 AIP Publishing LLC*. [http://dx.doi.org/10.1063/1.4899259]

I. INTRODUCTION

Large-scale motions in wall-bounded flows have received considerab attention since the late fifties, when Townsend[1] and Grant[2] realized that the long tails of time-delayed streamwise velocity autocorrelations[3] implied large structures carrying a substantial part of the kinetic energy. Examples are velocity streaks,[4] Reynolds-shear-stress structures,[5] and bulges in the outer region of turbulent boundary layers.[6,7] The best-known among them are the alternating high- and low-momentum velocity streaks of the buffer layer, which were first visualized and described in the experiments of Kline *et al.*,[4] Bakewell and Lumley,[8] and Corino and Brodkey.[9] This near-wall region is nowadays fairly well understood,[10] but the pattern of alternating high- and low-speed fluid is not restricted to the buffer layer, and extends to the logarithmic region with dimensions of the order of the flow thickness.[11,12] An early review of the coherent structures of wall-bounded turbulence is Robinson,[13] although the low Reynolds numbers available at the time restricted its focus to the near-wall and outer regions of boundary layers. Even today, our understanding of the associated kinematics and dynamics remains limited, in spite of the numerous models that have been proposed.[14–17]

In this paper we present fully three-dimensional two-point statistics of a new zero-pressure-gradient turbulent boundary layer[18] up to $Re_\theta \approx 6600$ ($\delta^+ \approx 2000$), and compare them to turbulent

---

a) sillero@torroja.dmt.upm.es
b) jimenez@torroja.dmt.upm.es

channels at similar Reynolds numbers.[19,20] To some extent, this work is a continuation of the paper of Sillero, Jiménez, and Moser,[18] in which one-point statistics of the velocity and pressure were presented and discussed for the new simulation, and of the comparison of boundary layers and channels at lower Reynolds numbers in Jiménez *et al.*[21] Those two types of flows are used as archetypes of external and internal wall-bounded flows, respectively. They are compared at constant Kármán number, $\delta^+ = u_\tau \delta/\nu$, defined in terms of the kinematic viscosity ν, the streamwise-dependent friction velocity u_τ, and the flow thickness δ. The latter is taken to be the 99% thickness in boundary layers, and the half-width in channels.[22] The "+" superscript denotes normalization with u_τ and ν. The Reynolds number $Re_\theta = U_\infty \theta/\nu$ is defined for boundary layers in terms of the momentum thickness θ and of the free-stream velocity U_∞. Throughout the paper, the velocity components in the streamwise (x), wall-normal (y), and spanwise (z) directions are u, v, and w, respectively, and the kinematic pressure p incorporates the constant fluid density. We often classify results as relating to the buffer, logarithmic, or outer regions, arbitrarily defined as $y^+ < 80$, $80\nu/u_\tau < y < 0.2\delta$, and $y > 0.2\delta$, respectively, and pay special attention to the last two regions. To our knowledge, this is the first detailed comparison between boundary layers and channels at moderately high Reynolds numbers using fully three-dimensional correlation functions.

Historically, the early one-dimensional correlations obtained by Grant[2] to investigate the large-scale structures in several turbulent flows were first extended by Tritton,[23] who compared his boundary layer with the channel in Ref. 24. He found no differences between the near-wall region of the two flows, and observed that the correlation length of the streamwise velocity greatly exceeds the distance to the wall, supporting Townsend[25] attached-eddy model. He also found that that length decreases above the logarithmic layer.[26–29] A similar effect was later found for internal flows,[30–32] although the length of the structures starts to decrease in this case beyond the middle of the outer region. Using large-eddy simulations of channels ($\delta^+ \approx 640$) in relatively short and narrow boxes, Moin and Kim[33] found that the one-dimensional streamwise velocity correlation in the flow direction extended over much longer distances than for the transversal velocity correlations when measured at four heights, spanning from the near-wall to the center of the channel, in agreement with previous numerical results.[34] Further analysis of the streamwise velocity correlation in the near-wall region was shown to be compatible with the elongated streaky structures previously reported in several experimental works.[4,8,9] The authors extended their work in Ref. 35 to include one-dimensional correlations of the vorticity fluctuations, and analyzed these one-dimensional correlations along two different inclined lines at ±45° to the wall, supporting a flow model consisting of dominant vortical structures inclined at 45°.

The reasons for the differences between internal and external flows are still unclear, and several explanations have been proposed. For instance, Ganapathisubramani *et al.*[26] computed velocity correlations at several heights of an experimental boundary layer ($\delta^+ \approx 1000$), and found differences in the length of the structures of the streamwise velocity with respect channels.[31] They argued that a significant part of the outer layer of channels behaves as if it were logarithmic, while boundary layers are contaminated in this region by the "wake" component, which they attributed to the interactions with the potential free stream. Similar conclusions were reached in Ref. 21 from the detailed examination of a numerical data base, and could explain both the observed locations for the maximum correlation lengths, and the longer structures in channels.

Accurate experiments and simulations of the largest scales in the logarithmic region have only become possible in the last decades, due in part to the high Reynolds numbers required to observe that region.[36] Nowadays, spatial flow reconstructions are commonly obtained experimentally by particle image velocimetry (PIV), although rarely in more than planar sections. For instance, Adrian, Meinhart, and Tomkins[37] conducted measurements of a turbulent boundary layer ($\delta^+ \approx 2000$), and found streamwise velocity structures as long as 2δ that were tilted from the wall[38] by about 12°. They explained them as "hairpin packets"[37,39] in which a collection of hairpins of size $\mathcal{O}(\delta)$ align with each other and propagate with small velocity dispersion. As a result, they create the longer streamwise structures of length $\mathcal{O}(10\delta\text{–}20\delta)$ that have been detected from spectral measurements, both experimentally and numerically.[20,29,40,41]

Liu, Adrian, and Hanratty[42] compiled two-dimensional spatial correlations in an experimental turbulent channel ($\delta^+ \approx 1400$) to study the structure of the velocity fluctuations and of the Reynolds shear stress. They observed correlation lengths of at least 2δ–4δ for the streamwise velocity along the flow direction, and much shorter ones for the wall-normal velocity, 0.3δ–0.4δ. The interaction between the streamwise and wall-normal velocities, described by their cross-correlation, revealed that the long structures carried a significant fraction of the Reynolds shear stress, but little energy in the wall-normal component. Other experimental investigations on the structure of the turbulent velocities using spatial correlations are those of Ganapathisubramani *et al.*[26] and Wu and Christensen[43] for boundary layers. Unfortunately, all the above PIV experiments are restricted to fairly short windows of streamwise size $\mathcal{O}(\delta)$. To overcome this limitation, other investigators have used techniques such as hot-film,[12,44] multisensor hot-wire anemometry,[29,45–47] or PIV in conjunction with Taylor hypothesis,[48] which allow two- and three-dimensional flow-reconstructions over longer extents at the expense of extra hypotheses.

Direct numerical simulations (DNS) provide high-quality databases with very good spatial and velocity dynamic ranges.[20,27,28,32,40,49–51] They often include two-point spatial correlations and spectra which, in contrast to experiments, can easily be made three-dimensional. For instance, the first available three-dimensional velocity correlations were computed by Moin and Moser[52] in the late eighties, using a channel flow at low Reynolds number ($\delta^+ \approx 180$). The extra information has often led to different models than those from experiments. For example, del Álamo *et al.*[17] found long conditional low-velocity structures in the wake of vorticity clusters, spreading conically downstream as in the attached-eddy model of Townsend,[14] but concluded that the vortices were organized by the wake, rather than the other way around.[53] Lee and Sung[27] simulated a boundary layer ($\delta^+ \approx 1000$), and reported correlation lengths as long as $\mathcal{O}(6\delta)$ for the streamwise velocity at the outer edge of the logarithmic region, inclined away from the wall by about 15°–20°. They extended their analysis to numerical pipes at similar Reynolds number,[32] finding longer structures than in boundary layers. The largest differences were located, as in the case of the channel, near the middle of the outer region.

In our study, spatial velocity and pressure correlations are computed within fairly long domains, $\mathcal{O}(20\delta)$, to allow the fluid structures to fully decorrelate and to observe the largest scales present in the flow. The Reynolds number is carried up to $\delta^+ \approx 2000$. Particularly interesting are the two-point statistics of the pressure fluctuations, which are generally harder to obtain experimentally than the velocities. Power spectra of the pressure at the wall have been available for some time, both from experiments[54] and from simulations,[55,56] but it is only recently that experiments away from the wall have become available.[57] Even in the case of DNS, less information is often reported for the pressure than for the velocities, but one- and two-dimensional spectra at all wall distances are also available.[21,22,58] During the refereeing of the present paper, Shinde, Laval, and Stanislas[59] published three-dimensional pressure and velocity correlations in the near-wall region of two numerical channels with and without pressure gradients, at $\delta^+ \approx 950$. To our knowledge, the three-dimensional pressure correlations presented here are the first available in the literature for the logarithmic layers of turbulent boundary layer and channel flows.

The article is organized as follows. Section II briefly describes the simulations and defines the post-processing procedures. The two-point correlations of the velocity are discussed in some detail in Sec. III, both for turbulent boundary layers and for channels, followed by the results for the cross-correlation of u and v in Sec. IV and of the pressure in Sec. V. Section VI describes conditional correlations, and Sec. VII summarizes and concludes.

II. NUMERICAL DATABASES AND METHODS

Table I summarizes the parameters of the direct numerical simulations used in this paper. In particular, we use previously published channels from our group at $\delta^+ = 934$ (CH950),[19] and $\delta^+ = 2003$ (CH2000),[20] together with a turbulent boundary layer (BL6600) in the same range of Reynolds numbers, $\delta^+ \approx 980$–2025.[18]

The numerical code for the channels integrates the Navier–Stokes equations in the form of an evolution problem for the wall-normal vorticity ω_y and for the Laplacian of the wall-normal velocity $\nabla^2 v$.[49] The spatial discretization uses Fourier expansions in the two wall-parallel directions, fully dealiased using the 2/3 rule. CH950 uses Chebychev polynomials in the wall-normal direction,

TABLE I. Parameters of the numerical simulations used in the text. L_x, L_y, and L_z are the box dimensions along the three axes, and N_x, N_y, and N_z are the collocation grid sizes. The corresponding resolutions, measured at the middle of the computational box, are ℓ_x, ℓ_y (measured at $y = \delta$), and ℓ_z. N_f is the number of fields used to accumulate statistics, T is the time spanned by those fields, and N_{cor} is the number of wall-normal locations at which correlations are compiled. The boundary layer properties, δ and u_τ, are taken at the middle of the box.

Case	Re_θ	δ^+	$(L_x, L_y, L_z)/\delta$	$\ell_x^+, \ell_y^+, \ell_z^+$	N_x, N_y, N_z	N_f	N_{cor}	Tu_τ/δ
CH950	...	934	8π, 2, 3π	9.2, 7.6, 3.8	3072, 385, 2304	74	112	12
CH2000	...	2003	8π, 2, 3π	8.2, 8.9, 4.1	6144, 633, 4608	233	34	11
BL6600	2780–6650	980–2025	21π, 3.5, 3.2π	6.5, 10.2, 3.8	15 361, 535, 4096	212	22	11.5

whereas CH2000 uses seven-point compact finite differences. Further numerical details can be found in the original publications.

The boundary layer is simulated in a parallelepiped over a flat plate with periodic spanwise boundary conditions and non-periodic streamwise and wall-normal directions. The numerical code solves the primitive-variable formulation of the incompressible Navier-Stokes equations, using a fractional-step method to ensure mass conservation.[60] Staggered three-points compact finite differences[61] are used for the spatial discretization of the derivatives in the x and y directions, except for the Poisson equation for the pressure, for which second-order finite differences are used. The representation in the spanwise direction is dealiased Fourier. A detailed description of the problem formulation, the numerical scheme, and its validation can be found in Simens *et al.*[62] The parallelization and implementation strategies are discussed in Borrell, Sillero, and Jiménez,[63] and the one-point statistics of the boundary layer are described in Sillero, Jiménez, and Moser.[18] The time marching for all the simulation codes is semi-implicit three-step Runge–Kutta.[64]

A. Two-points statistics

The paper discusses the average three-dimensional organization and structure of the flow in terms of spatial two-point correlation functions. For convenience, correlations are computed in Fourier space for all the homogeneous directions, and transformed to physical space whenever required for comparing different flows. For instance the covariance in boundary layers is defined as

$$\widehat{R}_{\psi\phi}(x, x', y, y', k_z) = \langle \widehat{\psi}(x, y, k_z)\widehat{\phi}^*(x', y', k_z)\rangle, \tag{1}$$

where ψ and ϕ are generic variables of zero mean, $\widehat{\psi}$ stands for Fourier transformation with respect to z, and $\langle \cdot \rangle$ is the expected value. The asterisk is complex conjugation, and k_z is the spanwise wave number. In streamwise-homogeneous channels, the covariance reduces to $\widehat{R}_{\psi\phi}(\Delta x, y, y', k_z)$, where $\Delta x = x - x'$, and can be computed directly in terms of the streamwise wavenumber k_x. In all cases, the covariance in physical space, $R_{\psi\phi}(x, x', y, y', \Delta z)$, is obtained as the inverse Fourier transform of $\widehat{R}$, where $\Delta z = z - z'$ is the distance between the two points in the homogeneous spanwise direction.

The autocorrelation coefficient,

$$C_{\psi\phi}(\mathbf{r}, \mathbf{r}') = R_{\psi\phi}(\mathbf{r}, \mathbf{r}')/\sigma_\psi(\mathbf{r})\sigma_\phi(\mathbf{r}'), \tag{2}$$

is obtained by normalizing the covariance with the product of the standard deviations at the two points involved in the measurements, denoted by $\mathbf{r'}$ for the reference point and by $\mathbf{r}$ for the moving one. This is the normalization adopted by most researchers,[23,26–28,42,43] although the normalization of $R_{\psi\psi}$ with $\sigma_\psi(\mathbf{r}')^2$ is also used occasionally.[46,65] Statistically, the definition (2) has a well-defined interpretation, and is known to be asymptotically unbiased.[66] For example, it can be shown by direct calculation that the expected relative error in the least-square fit of $\psi(\mathbf{r})$ as a function of $\phi(\mathbf{r}')$ is $\varepsilon^2/\sigma_\psi^2(\mathbf{r}) = 1 - C_{\psi\phi}^2$. We have tested the effect of using both normalizations, and found only minor differences in the resulting correlations, mostly associated with the effect of the small standard deviations near the outer edge of the boundary layer. From now on, we will refer to the correlation coefficient defined in (2) as correlation, unless otherwise stated.

Covariances are accumulated over the number of flow fields specified in Table I. Since boundary layers are not homogeneous in the streamwise direction, correlations are only compiled at three reference sections, chosen so that $\delta(x')^+ = 1313$, 1530, and 1990. In each case, the streamwise range is $x = x' \pm 10\delta$, except for the most downstream location, where the computational box ends at $x_{end} \approx x' + 2\delta$. Inspection of the resulting velocity and pressure correlations reveals that they typically decay within such domains to below a few percent, which is also the order of their statistical uncertainty. This suggests that the largest scales of the flow are properly captured.[22,67] To decrease noise, the covariances and standard deviations in boundary layers are averaged over windows $x' = x'_{nom} \pm \delta/2$ around their nominal reference position x'_{nom}, keeping Δx constant. This produces smoother correlations while keeping the systematic error small.[21] The correlations in channels are computed over the whole computational box, $x = x' \pm 4\pi\delta$, which corresponds to a domain similar to those used in the boundary layer. In all cases, the correlations are compiled for a range of different heights distributed over the inner, logarithmic, and outer regions of the flow (see Table I).

III. VELOCITY CORRELATIONS

One of the "advantages" of numerical simulations over experiments is that an adequate representation of the problem requires that the domain size should contain the largest relevant flow structures. The observational domain is therefore not generally a limiting factor, although at the cost of considerable computational expense. In the present case, this will allow us to spatially characterize turbulent structures with lengths of the order of $\mathcal{O}(20\delta)$, which have only previously been reported in experiments in terms of passing times.[29,68]

Figure 1 is a three-dimensional representation of C_{uu} for the boundary layer, centered in the outer region, $y'/\delta = 0.6$, and $\delta(x')^+ = 1530$. The domain in the figure is $6\delta \times 1.2\delta \times 2\delta$ in the streamwise, wall-normal, and spanwise direction, respectively, which corresponds to the central part of the larger correlation box ($20\delta \times 3.4\delta \times 10\delta$). In describing the size of the correlations we will use L_j^m to denote the maximum distance between points of a given three-dimensional correlation isosurface along the j direction, even if those points are not at the same distance from the wall, where j may vary from x to z (see Fig. 8). We will reserve L_j for the length of the one-dimensional section

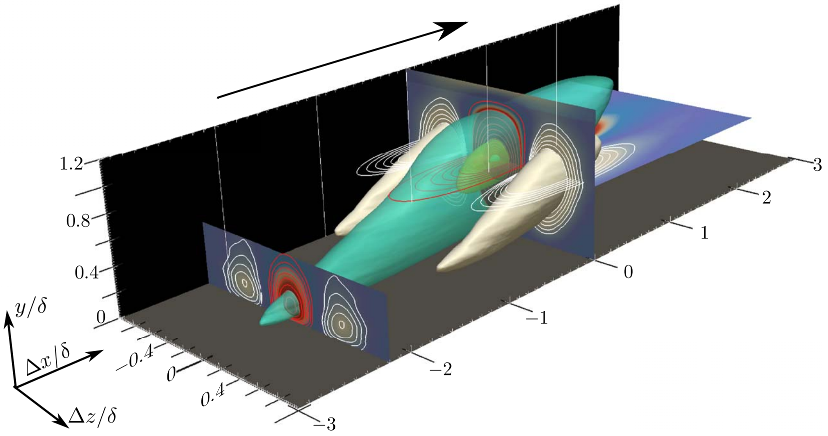

FIG. 1. Three-dimensional representation of the correlation of the streamwise velocity fluctuations, C_{uu}, for a boundary layer at $\delta^+ = 1530$ and $y'/\delta = 0.6$. The flow goes from left to right. Several isosurfaces are shown at $C_{uu} = -0.09$ (white), $+0.09$ (turquoise), $+0.4$ (yellow), and $+0.8$ (blue). For the last three isosurfaces a transparency of 40% is set. In the planes going through the correlation origin, the contour lines of positive and negative correlation values are colored red and white, respectively, ranging from 0.09 to 1.0 and from −0.04 to −0.1. The contour lines of the zy-plane at $\Delta x/\delta = -2.2$ range from 0.03 to 0.1, and from −0.02 to −0.06. Cuts are colored by the correlation value, ranging from red (most positive) to white (most negative), passing through blue (zero).

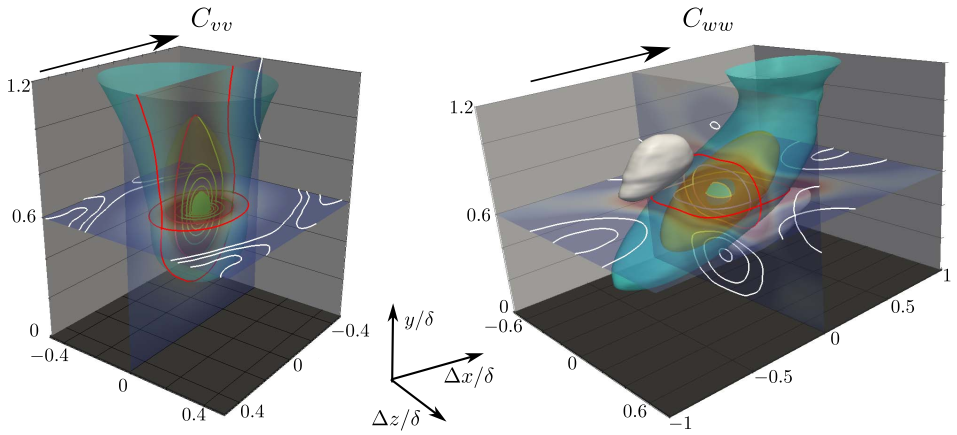

FIG. 2. Three-dimensional representation of the correlation of the wall-normal velocity fluctuations, C_{vv}, and of the spanwise velocity fluctuations, C_{ww}, for a boundary layer at $\delta^+=1530$ and $y'=0.6\delta$. The flow goes from left to right. Several isosurfaces are shown at $C=-0.09$ (white), $+0.1$ (turquoise), $+0.2$ (yellow), and $+0.6$ (blue). For the last three isosurfaces a transparency of 40% is set. In the planes going through the correlation origin, the contour lines of positive and negative correlation values are colored red and white, respectively, ranging from 0.1 to 1.0 for both correlations, from -0.01 to -0.02 in C_{vv}, and from -0.02 to -0.08 in C_{ww}. A transparency of 40% is set for these planes. Cuts are colored by the correlation value, ranging from red (most positive) to blue (most negative), passing through white (zero).

of the isosurface along the j axis. For the isosurface $C_{uu} = 0.09$, there is a positively correlated region extending about $L_x^m \approx 4\delta$ between its farthermost points in the streamwise direction, from 3δ upstream to δ downstream of the reference point. In the wall-normal and spanwise directions, its size is $L_y^m \approx \delta$ and $L_z^m \approx 0.5\delta$, respectively. Two negatively correlated regions flank the positive one, separated from each other by $\Delta z \approx \delta$. Their $C_{uu} = -0.09$ isosurfaces are shorter than the positive one, $L_x^m \approx 1.7\delta$, and are also smaller in the wall-normal and spanwise directions: $L_y^m \approx 0.55\delta$ and $L_z^m \approx 0.35\delta$. Both the positive and negative regions are slightly inclined with respect to the wall, as will be quantified in Sec. III C.

Some weaker correlation isocontours are included in Fig. 1 in the form of two-dimensional sections. Two of them pass through the origin ($y = y'$ and $x = x'$), and a third is an upstream cross plane at $\Delta x/\delta = -2.2$.

Note that the form of the correlations in those sections is not completely arbitrary. Townsend[14] showed that it follows from incompressibility that the covariance must satisfy $\sum_j \partial_j R_{ji}(\mathbf{r}, \mathbf{r}') = 0$, where ∂_j is the derivative with respect to r_j, and j refers to the coordinate direction or to the corresponding velocity component. Integrating over the whole domain, and noting that the correlation vanishes at large $|\mathbf{r} - \mathbf{r}'|$, or whenever $\mathbf{r}$ is at a no-slip wall, it follows that

$$\iint R_{uu}\,\mathrm{d}z\,\mathrm{d}y = \iint R_{vv}\,\mathrm{d}x\,\mathrm{d}z = \iint R_{ww}\,\mathrm{d}x\,\mathrm{d}y = 0. \tag{3}$$

The integrations in (3) are over a full plane normal to each velocity component: from $(-\infty, \infty)$ in the case of x and z; from one wall to the other in the case of y in channels; and from the wall to the potential stream in the case of y in the boundary layer. Therefore, the correlation flux over planes orthogonal to a given velocity component has to vanish, implying the coexistence of positive and negative correlation regions within each plane. This can be seen in Fig. 1 for the two cross-flow sections of C_{uu}. Note that (3) does not require the plane to pass through the origin, and that it does not apply strictly to the correlation coefficient in inhomogeneous flows, because of the spatial dependence of the standard deviations.

Figure 2 displays the three-dimensional correlations of the transversal velocities, C_{vv} and C_{ww}, taken at the same height and Reynolds numbers as in Fig. 1. The domains displayed in the figure are shorter than in Fig. 1, but not much narrower: $\delta \times 1.2\delta \times \delta$ for C_{vv}, and $2\delta \times 1.2\delta \times 1.5\delta$ for C_{ww}.

C_{vv} is a tall structure elongated in the wall-normal direction. In the wall-parallel (xz) plane, the section of the positively correlated region is elliptical, with the major axis at $C_{vv}=0.1$ aligned in the free-stream direction, and axes lengths $a_x \approx 0.55\delta$ and $a_z \approx 0.4\delta$. Weaker negatively correlated regions are found outside the ellipse $C_{vv} = -0.01$, with axes $a_x \approx 1.5\delta$ and $a_z \approx 0.8\delta$. The most intense anticorrelated regions form a quadrupole centered at $\Delta z \approx \pm 0.4\delta$ and $\Delta x \approx \pm 0.5\delta$, which we will see later to be specific to this wall distance.

The spatial organization of C_{ww} is particularly interesting. It consists of a positively correlated region inclined with respect to the wall at a steeper angle than the one of C_{uu}, flanked by four negatively correlated regions. The strongest anticorrelated regions are the white isosurfaces $C_{ww} = -0.09$ above and below the positive one. Barely visible in the figure are two weaker negative objects in the spanwise direction. One consequence of this quadrupole structure is that the intersections of the positive correlation isosurface with the xz- and zy-planes are characteristically squarish for C_{ww}, rather than elliptical (see Fig. 4(f)). Only the intersections with the longitudinal xy-plane are elliptical. The dimensions of $C_{ww} = 0.1$ in the xz- and zy-planes are $L_x \approx L_z \approx 0.65\delta$ and $L_y \approx 0.35\delta$. The length of the negative objects for $C_{ww} = -0.09$ is $L_x^m \approx 0.5\delta$ for the object located at the top, and $L_x^m \approx 0.65\delta$ for the one at the bottom, both with wall-normal size $L_y^m \approx 0.3\delta$.

In summary, the spatial organization of the two velocity correlations in Fig. 2 is that the negatively correlated regions of w are above and below the origin, while those of v are located spanwise. It suggests that, at least at this distance from the wall, the dominant structures of the velocity is a quasi-streamwise roller inclined with respect to the wall, rather than a spanwise one.

A. Two-dimensional sections

We next discuss two-dimensional sections of the velocity correlations, taken through the origin, centering initially on one location in the lower logarithmic layer, $y' \approx 0.1\delta$ ($y^+ \approx 200$), and another one in the outer region, $y' \approx 0.8\delta$. Two-dimensional sections of the three-dimensional correlations correspond to one-dimensional energy spectra, in that they include integrated information from all the scales along the direction being discarded. Therefore, they are easier to compare with experimental information than the full three-dimensional object. For example,

$$R_{\psi\phi}(x, x', y, y') \equiv R_{\psi\phi}(x, x', y, y', \Delta z = 0) = \int \widehat{R}_{\psi\phi}(x, x', y, y', k_z)\, \mathrm{d}k_z. \tag{4}$$

The streamwise (xy) sections of C_{uu} and C_{ww} are given in Fig. 3, and show that C_{uu} is longer than C_{ww} at the two chosen heights (note the different horizontal scales of the left and right columns of the figure). Figures 3(a) and 3(b) present the correlations at $y' \approx 0.1\delta$ for boundary layers. They show inclined structures of length $L_x^m \approx 8\delta$ for C_{uu}, and $L_x^m \approx 1.5\delta$ for C_{ww}.

More interesting are Figs. 3(c)–3(f), farther from the wall. They clearly show that structures in channels are longer than boundary layers, specially for C_{uu} in Figs. 3(c) and 3(e). This agrees qualitatively with published spectra,[21] but it is important to understand that correlations and spectra are not strictly equivalent. In the first place, streamwise spatial spectra in inhomogeneous boundary layers can only be defined approximately.[21] Second, a spectrum at a fixed y, or even a set of spectra at several heights, contain different information from that in a two-dimensional correlation. Consider, for example, C_{ww} in Fig. 3(d). Taking as a reference the isocontour $C_{ww} = 0.05$, any analysis involving only $y = 0.8\delta$ would suggest correlations lengths of the order of $L_x \approx 0.7\delta$, while the two-dimensional correlation shows that the structure is longer. The maximum streamwise distance, $L_x^m \approx 2.5\delta$, is between points at different heights, because the structure is relatively thin but long and inclined forwards. Figures 3(a), 3(c), and 3(e) show that the effect is also present in C_{uu}, although less marked.

Centering on the same correlation isocontour for the streamwise velocity at $y' = 0.8\delta$, $C_{uu} = 0.05$ extends for $L_x^m \approx 6\delta$ in boundary layers, and for $L_x^m \approx 15\delta$ in channels. In the wall-normal direction, C_{uu} spans the whole flow thickness, from very close to the wall to either the potential stream or to beyond the channel centerline, whereas C_{ww} is flatter. Both correlations are inclined forwards, presumably as a consequence of the shearing by the mean velocity profile. Figure 2 shows that C_{vv} is essentially perpendicular to the wall.

Very long features have been reported in the logarithmic and outer layers of all wall-bounded flows, variously referred to as "largest,"[11] "very large,"[12] or "global."[19,40] They are known to

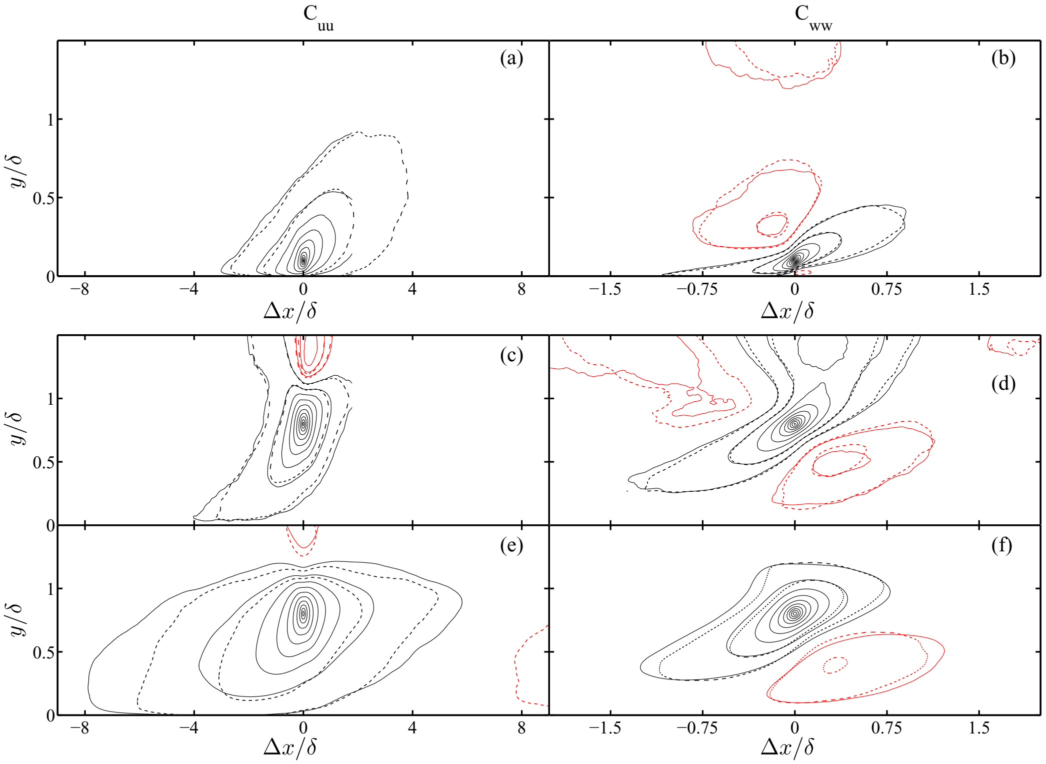

FIG. 3. Streamwise (xy) sections of the correlations at: (a) and (b) $y'/\delta = 0.1$, and (c)–(f) $y'/\delta = 0.8$. Left column is C_{uu}, and right column is C_{ww}. (a)–(d) Boundary layers. (e) and (f) Channels. Positive contours (black) are (0.05:0.1:...), and negative ones (red) are (−0.05:−0.05:...). ——, $\delta^+ \approx 2000$; - - - -, boundary layer at $\delta^+ = 1313$, and CH950. Note the different aspect ratios of the two columns of panels. Flow is from left to right.

be correlated across the full boundary layer thickness,[19,30] and to penetrate the sublayer.[20,30,40] The streamwise lengths given for C_{uu} in boundary layers are typically of the order of $\mathcal{O}(4\delta$–$5\delta)$, independent of the Reynolds number,[27,29,46] while those in channels and pipes tend to be closer to $\mathcal{O}(9\delta$–$20\delta)$.[19,30,40,67] Those numbers are in general agreement with Figs. 3(c) and 3(e). On the other hand, Hoyas and Jiménez[69] surveyed u-spectra from a wide variety of flows, including experimental and atmospheric boundary layers, and found evidence for structures of the order of 20δ in most of them. Hutchins and Marusic[29] presented visual evidence for essentially infinite streaky u-structures in boundary layers, and showed that the shorter correlations and spectra could be explained by their meandering, rather than by their intrinsic length. Different correlation lengths could thus depend on the property being measured.

It is interesting that the near-wall correlations at $y' = 0.1\delta$ in Figs. 3(a) and 3(b) are not much shorter than those at $y' = 0.8\delta$,[23] in agreement with the previously mentioned evidence that energy from the larger outer structures reaches the near-wall layer.[20,70,71] In fact, the horizontal dimensions in Figs. 3(c) and 3(d) constrain those in Figs. 3(a) and 3(b). It follows from (2) that $C(y, y', x, x') = C(y', y, x', x)$, so that, if the correlations centered far from the wall extend into the inner layer, those centered near the wall must extend into the outer layers with comparable streamwise dimensions. For example, neglecting the streamwise inhomogeneity of the boundary layer, the correlation along $y = 0.1\delta$ in Fig. 3(c) is the x-reflection of the correlation along $y = 0.8\delta$ in Fig. 3(a), and their streamwise dimensions must be identical.

One of the consequences of that reciprocity is that, except in strictly symmetric cases, a correlation that is biased downstream from the reference point near the wall corresponds to a backward-biased one far from the wall. For example, as y' moves away from the wall from Fig. 3(a) to Fig. 3(e), the upstream end of C_{uu} gets longer, while the downstream one gets shorter. We will see in Sec. III C that this is part of a continuous trend, in essence because all the correlations in that

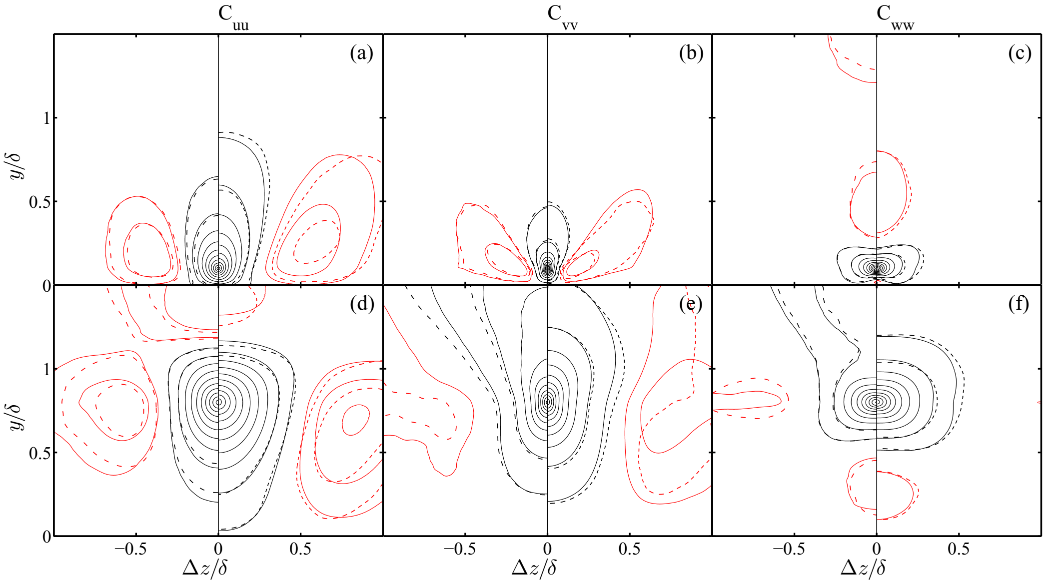

FIG. 4. Cross-flow (zy) sections of the correlations at: (a)–(c) $y'/\delta = 0.1$, and (d)–(f) $y'/\delta = 0.8$. (a) and (d) C_{uu}; (b) and (e) C_{vv}; (c) and (f) C_{ww}. For each panel, the left side are boundary layers, and the right side are channels. Positive and negative contours are colored in black and red, respectively. The positive contours (black) are (0.05:0.1:...). In (a), (c), (d), and (f), the negative contours (red) are (−0.05:−0.05:...). In (b) and (e), they are (−0.01:−0.02:...). In all panels: ——, $\delta^+ \approx 2000$; - - - -, boundary layer at $\delta^+ = 1313$, and CH950.

range of wall distances represent, at least in part, different aspects of the same large-scale structure extending from the top of the buffer layer to the outer edge of the flow.

In contrast to the streamwise sections, Fig. 4 shows that the spatial organization of the correlations in the cross-flow (zy) plane is qualitatively similar for boundary layers and channels. Note that, because the correlations in this plane are symmetric with respect to z, the two flows are shown side-by-side in each panel, with boundary layers on the left and channels on the right.

The streaky pattern of the u-structures is revealed in Figs. 4(a) and 4(d), with alternating low- and high-momentum regions separated by distances of the order of δ. As in the case of the streamwise sections, C_{uu} is also the correlation in which channels differ more from boundary layers, with the longer streaks of the channels associated to somewhat wider and taller cross-sections. It is interesting that, although the streak separation gets wider with increasing wall distance, it grows more slowly than proportionally to y'.

This is more clearly seen in the right-hand side of Figs. 5(a) and 5(d), which contains one-dimensional spanwise sections of C_{uu} as functions of z and $y = y'$. The growth of the negative correlation contours is roughly linear in y below $y \approx 0.9\delta$, but with a relatively large intercept at $y = 0$. Reference 16 found a similar result for the width of the low-momentum regions in a boundary layer, $L_z \approx 0.1\delta + 0.75y$ below $y/\delta = 0.25$. This growth rate is faster than the one for y/δ in 0.1–0.9 in Fig. 5(d), but agrees approximately with the near-wall boundary between positive and negative correlations in that figure. Note that the dashed and solid lines in Fig. 4 correspond to two Reynolds numbers separated by a factor of 1.5, and that their rough agreement suggests that the streak spacing scales in outer units. In fact, the reciprocity discussed above for Figs. 3(a) and 3(c) also applies to the cross sections of any wall-attached structure, such as those of u. If the wall-parallel dimensions of the correlations scale in outer units far from the wall, they should do the same near it.

The sections of C_{vv} in Figs. 4(b) and 4(e) are narrower than those of C_{uu} near the wall, although the dimensions of the two variables are much closer to each other in the outer layer. Figures 4(b) and 4(e) confirm that C_{vv} is not attached to the wall.[25] The contours in Fig. 4(b) do not extend into the outer layer, and those in Fig. 4(e) do not reach the wall. Reciprocity cannot therefore be invoked, and the scale of C_{vv} varies strongly with y', as repeatedly shown, for example, by spectral measurements.[10] It will be seen below, when discussing Fig. 5, that the spanwise separation of the

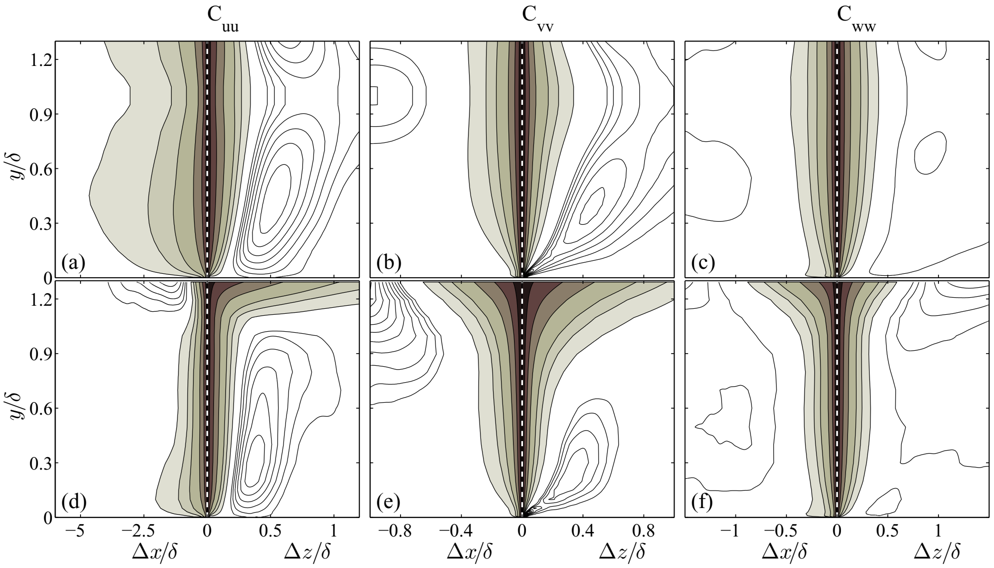

FIG. 5. Single-height ($y = y'$) sections of the velocity correlations as functions of y'/δ for channels (in the top row) and boundary layers (bottom). $\delta^+ \approx 2000$. The left half of each panel is the upstream streamwise section ($\Delta z = 0$), and the right half is the spanwise one ($\Delta x = 0$). (a) and (d) C_{uu}. (b) and (e) C_{vv}. (c) and (f) C_{ww}. For all panels, the shaded contours are positive correlations (0.1, 0.2, 0.3, 0.5, 0.7, 0.9). For C_{uu} and C_{ww}, the negative line contours are (-0.02:-0.03:...). For C_{vv}, they are (-0.01:-0.01:...).

"return" negative lobes of C_{vv} is roughly proportional to y in the logarithmic layer. Note that, although the continuity relation (3) requires the wall-parallel integrals of C_{vv} to vanish, its return lobes are weaker and wider than those of u and w, suggesting that either the v structures are formed by a central compact down(up)-wash surrounded by a more diffuse counter-flow, or the relative positions of neighboring counter-flowing structures is less ordered than for other velocity components.

The cross-sections of C_{ww} are shown in Figs. 4(c) and 4(f). Their positive lobes are thinner in the wall-normal direction than either C_{uu} or C_{vv}, but the full correlation, including positive and negative regions, spans a large fraction of the flow thickness. In this sense, this is also an attached variable,[25] and its wall-parallel dimensions vary relatively little with y'. On the other hand, its wall-normal thickness, which is unconstrained by reciprocity, grows linearly with the distance to the wall (see Fig. 10 in Sec. III C). As a consequence, the positive contours of C_{ww} are relatively flat near the wall, and more square away from it. It follows from the continuity condition (3) that the integral of C_{ww} should vanish over the streamwise xy-plane, and Figs. 3(b), 3(d), and 3(f) show that the cancellation takes the form of alternating relatively thin layers stacked in the wall-normal direction. The intersection of these inclined layers with the cross plane appears in Figs. 4(c) and 4(f) as negative lobes above or below the primary positive contours. As already mentioned, the combination of Figs. 4(b) and 4(e), and Figs. 4(c) and 4(f) suggests a quasi-streamwise roller with dimensions of order δ, which the streamwise sections in Fig. 3 show to be inclined with respect to the wall. Note that the discussion in this section does not refer to structures in the buffer region. The reference heights of the correlations in Fig. 4 are $y'^+ = 200$ and $y'^+ = 1600$. The cross-flow dimensions of these rollers, as measured by the distance from the reference point to the first negative minimum of the correlation, are relatively constant at $L_y \approx 0.5\delta$ in the wall-normal direction for C_{ww}, and grow from $L_z \approx 0.2\delta$ at $y'/\delta = 0.1$ to $L_z \approx 0.9\delta$ at $y'/\delta = 0.8$, for C_{vv}. As in the case of the cross-sections of the u-streaks, the agreement of the two Reynolds numbers in Fig. 4 suggests that the roller dimensions scale in outer units.

Figure 5 contains one-dimensional sections of the correlations at $y = y'$, and summarizes the dimensions of the three velocity correlations. As in the case of Fig. 4, the exact or approximate symmetries of the flow allow us to include in the figure the three velocity components, which are separated into the three columns of panels, the two flows, with the channel in the upper row and the boundary layer in the lower one, and both the streamwise sections ($\Delta z = 0$) on the left half of each

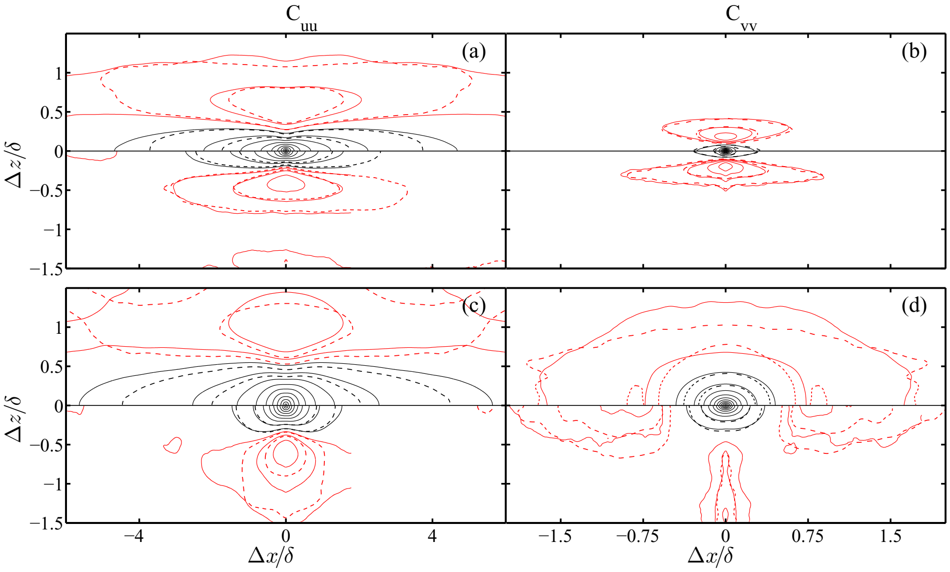

FIG. 6. Wall-parallel (xz) sections of the correlations at (a) and (b) $y'/\delta = 0.1$, and (c) and (d) $y'/\delta = 0.8$. (a) and (c) C_{uu}; (b) and (d) C_{vv}. For each panel, top are channels, and bottom are boundary layers. Positive contours (black) are (0.05:0.1:...). Negative contours (red) are (−0.01:−0.05,...) for C_{uu}, and (−0.01:−0.01:...) for C_{vv}. In all panels: ——, $\delta^+ \approx 2000$; - - - -, boundary layer at $\delta^+ = 1313$, and CH950. Note the different aspect ratios of the two columns of panels. Flow is from left to right.

panel, and the spanwise sections ($\Delta x = 0$) on its right half. In those cases in which the symmetry is only approximate, such as in the streamwise sections of the boundary layer, only the upstream part of the correlation is included, but it was checked that there are no qualitative differences with the downstream part. The lower row of Fig. 5 extends slightly above $y = \delta$, to show how the turbulent flow merges into the mostly potential free stream. The channel in the upper row is statistically symmetric with respect to $y = \delta$, but the domain is kept as in the boundary layer to facilitate comparisons.

In all panels, there is a clear distinction between a near-wall region below $y/\delta = 0.2$–0.3, where the correlations grow wider and longer, and a layer above it, where the dimensions either remain constant or decrease slightly. Another transition takes place above $y \approx \delta$ in the boundary layers, where all the correlations grow rapidly in size, clearly because the small rotational scales die rapidly above the turbulent interface, and the larger potential structures predominate.

A more interesting transition occurs around $y/\delta \approx 0.6$ in boundary layers. Consider C_{vv} in Fig. 5(e). Below $y/\delta = 0.6$ the negative lobe of the correlation is in the spanwise direction, on the right-hand side of the panel. Above that level, that lobe disappears, and is substituted by another one in the streamwise direction (on the left-hand side of the panel). At the same time, the spanwise dimensions of the positive lobe begin to widen, and its aspect ratio switches from streamwise to spanwise elongation.[26] A similar transition occurs around $y/\delta = 0.8$ in the channel, although in that case the spanwise negative lobe weakens but does not disappear. While these changes take place in v, the correlations of u and w also change. For example, C_{uu} in Fig. 5(d) shortens at the heights where the spanwise negative lobe of C_{vv} weakens, and its spanwise lobe, representing the spanwise alternation of streaks, also weakens. Eventually, a negative streamwise lobe also appears for C_{uu} near the edge of the boundary layer, and the structure of the correlations suggests a transition from a streamwise-oriented organization of the layer in the near-wall region, to a more isotropic, or spanwise-oriented, one far from the wall. The channel correlations in Fig. 5(a) can be interpreted as an incomplete version of the boundary layer transition, with C_{uu} shortening, as in the boundary layer, but without the appearance of a fully negative streamwise lobe.

Further detail of this behavior is presented in Fig. 6 with wall-parallel (xz) sections of C_{uu} and C_{vv}, revealing the more complex organization. As before, the spanwise symmetry of the correlations allows us to represent together the channels in the top part of each panel, and the boundary layers in the bottom. The two sections near the wall, Figs. 6(a) and 6(b), and the outer section of C_{uu} in Fig. 6(c), hold no surprises. They are consistent with the organization of the streamwise velocity into streamwise streaks alternating in the spanwise direction, and the corresponding organization of v into quasi-streamwise rollers. The already mentioned difference between the streamwise length of u in boundary layers and channels is also clearly visible. On the other hand, the wall-parallel sections of C_{vv} in Fig. 6(d) are qualitatively different from those closer to the wall. The lateral correlation minima in Fig. 6(b) are substituted by a roughly circular annular trough in the case of the channel, and by localized minima up- and down-stream from the central peak in the boundary layer. The quadrupole structure of the correlation minima in Fig. 2(a) is now seen to be a transitional stage between the spanwise structure of C_{vv} near the wall, and its streamwise organization in the outer layer. The transition is clearer in boundary layers, where the spanwise negative lobes of C_{vv} all but disappear far from the wall, but it is also present in the channel.

The behavior of C_{ww} in Figs. 5(c) and 5(f) is more difficult to interpret, because we know from Figs. 3(d) and 3(f) that its negative lobes are above and below the primary peak, rather than in front or to the side. They are therefore not captured well by the wall-parallel sections in Fig. 5. For example, the disappearance from the x-section of the negative correlation lobes towards the center of the channel, or near the edge of the boundary layer, simply means that the body of the correlation tends to be horizontal at those locations, from symmetry. In fact, most of the negative correlation contours in Figs. 5(c) and 5(f) are too weak to be visible in either of the cross sections in Figs. 3 or 4. The main exception is the strong spanwise negative peak in the upper-right corner of Fig. 5(f), whose main role is to satisfy continuity with the streamwise negative peak of C_{uu} in the upper-left corner of Fig. 5(a).

Another interesting feature is the near-wall "nose" of C_{ww}. Comparison of different Reynolds numbers (not shown) reveals that this is a buffer-layer feature, peaking about $y^+ = 15$, and scaling in wall units. It represents elongated narrow regions that are almost surely associated with the quasi-streamwise vortices in that part of the flow.[49]

The most striking difference is between the streamwise halves of Figs. 5(a) and 5(d) which show the length disparity between boundary layers and channels. What makes it interesting is that it extends over the whole flow thickness, including heights below $y/\delta = 0.4$ in which the effect of the intermittency in the outer edge of the boundary layer should be negligible. However, we have argued that the correlations of attached variables, such as u, are bound to be essentially uniform in y, because they represent different aspects of vertically correlated structures. We will see in Fig. 9 in Sec. III C that u is correlated across the flow thickness, both in boundary layers and in channels. Therefore, its relatively uniform streamwise length over the whole flow can be understood as an outer-layer effect in both cases, transmitted near the wall by the pressure fluctuations.[70]

B. The effect of box size and Reynolds number

Figures 3, 4, and 6 contain data from the two extreme Reynolds numbers of the present boundary-layer data set, which differ by a factor of 1.5. In general, they agree well, showing that the correlations scale in outer units at the two chosen wall distances.[29,46] More complete scaling results can be obtained by redrawing Fig. 5 for a wider range of Reynolds numbers. Although not shown here to avoid clutter, this was done for all the available channel simulations from our group ($\delta^+ = 350$–2000),[19,20,40] and for six stations of the present and earlier[21] boundary-layer simulations, covering $\delta^+ = 450$–1950. Where appropriate, they were supplemented by results from channels at $\delta^+ = 4200$ in a smaller box, and at $\delta^+ = 550$ in a very large one.[67] The results are summarized next.

The kink in the streamwise correlations of C_{vv} occurs at the top of the logarithmic layer, $y/\delta = 0.15$, for boundary layers and channels, and scales well in outer units. Above the kink, the correlation length at $C_{vv} = 0.1$ stabilizes at $L_x \approx 0.7\delta$. As already mentioned, the near-wall nose in C_{ww} is a viscous feature, scaling in wall units. The spanwise correlation C_{uu} generally scales in outer units, except for $y^+ \lesssim 30$, where both boundary layers and channels have a width $L_z^+ \approx 100$, clearly related to the sublayer streaks.[72] The streamwise sections of this correlation collapse near the wall in mixed units, L_x/δ vs. y^+, but they are different for the two flows. The boundary layers keep growing up to $y/\delta \approx 0.15$, where they stabilize at $L_x/\delta \approx 1.5$ for $C_{uu} = 0.1$. The channels are roughly

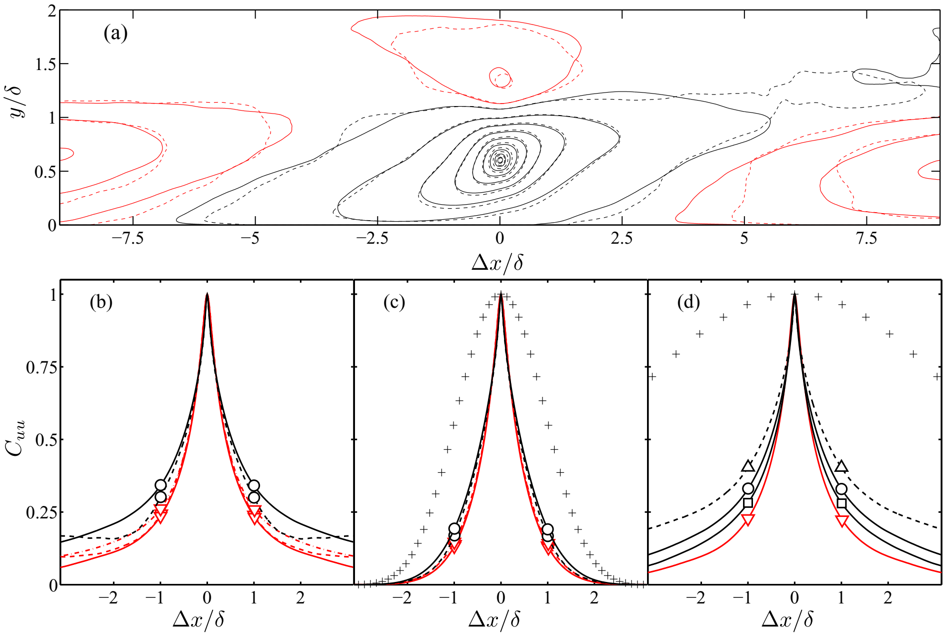

FIG. 7. Effects of the Reynolds number and computational box size on C_{uu} at $y'/\delta = 0.6$ in channels. (a) Filtered C_{uu}. A low-pass sharp Fourier filter is applied in the streamwise direction, with cut-off $\lambda_x^{co}/\delta = 8\pi$. Positive contours (black) are (0.02:0.1:...), and negative ones (red) are (−0.02:−0.05:...). ——, CH2000; - - - -, CH950. (b)–(d) Single-height ($y = y'$) streamwise ($\Delta z = 0$) correlations. Symbols stand for Reynolds numbers: ▽ (red), $\delta^+ \approx 550$; □, $\delta^+ \approx 950$; ○, $\delta^+ \approx 2000$; △, $\delta^+ \approx 4200$.[67] Lines stand for the length of the simulation box: - - - -, $L_x/\delta = 2\pi$; ——, 8π; — - —, 60π.[67] (b) No windowing. Different simulation boxes, and $\delta^+ = 550$ and 2000. (c) Same cases as in (b), with a data window of size $2\pi\delta$. (d) With a window of size $8\pi\delta$. $\delta^+ = 550$–4200. The symbol + is the Blackman-Harris[76] data window.

twice longer than the boundary layers at the same height, even in the buffer region, and keep getting longer up to $y/\delta \approx 0.5$.

The longitudinal sections of C_{uu} in channels are the exception to the scalings in the previous paragraph, in that they do not scale in outer (or wall) units even far from the wall. For example, reducing the Reynolds number by a factor of two in Fig. 3(e) reduces its length by 20%. The trend of shorter C_{uu} at lower Reynolds numbers continues for all the channels tested with similar box size, down to $\delta^+ = 350$. Liu, Adrian, and Hanratty[42] also found that the length of C_{uu} in channels depends on the Reynolds number ($\delta^+ = 300$–1400), but their results are different from ours. They find that increasing the Reynolds number leads to longer structures near the wall, and to shorter ones farther away, while the trend in our case is to longer correlations everywhere.

A failure in the Reynolds-number scaling of the streamwise velocity fluctuations far from the wall has been noted before.[19,22,73] At its simplest level, it manifests itself as an increase of u'^+ measured at a fixed y/δ as the Reynolds number increases, at least for $\delta^+ \lesssim 10^4$. The references just cited include several kinds of wall-bounded flows. Later measurements in boundary layers and pipes at much higher Reynolds numbers[74,75] suggest that this could still be a low-Reynolds-number phenomenon, but the question is still unsettled and the effect should be present at the Reynolds numbers discussed here. It has been shown before that the problem is related to the longest structures, because it mostly disappears when the spectra are filtered beyond $\lambda_x/\delta \approx 6$, both in numerics and in experiments.[19] This is also the case here. Figure 7(a) shows C_{uu} for the two channels used in Fig. 3(e), with their $k_x = 0$ modes removed by a sharp Fourier filter that only retains wavelengths $\lambda_x/\delta \leq 8\pi$. Most of the discrepancies have disappeared.

However, Fig. 3(e) is also the only one in which our correlations extend over dimensions comparable to the computational box, and it is important to clarify whether the effect is real or numerical.

Consider Fig. 7(b), which shows several one-dimensional streamwise correlations, C_{uu} from channels at $\delta^+ = 950$ and $\delta^+ = 2000$, with simulation boxes ranging from 2π to 60π. There is a substantial difference between the correlations from the different box sizes at the same Reynolds number, including the two boxes at $\delta^+ = 550$ with $L_x/\delta = 8\pi$ (red solid line) and $L_x/\delta = 60\pi$ (chain-dotted), even if both boxes are much longer than the range of separations shown in the figure. The simplest solution that comes to mind is to damp the edges of the data with a streamwise data window, $W(\Delta x)$ similar to those used in computing modified periodograms.[77] It is easy to see that this is equivalent to windowing the correlation with $W(\Delta x)$. Figure 7(c) displays the result of applying a Blackman–Harris data window[76] extending from $\Delta x/\delta = -\pi$ to π. It cures the problem, including the correlations in boxes of length $2\pi\delta$, which are minimal with respect to that window. The collapse of the two Reynolds numbers also confirms that there is little Reynolds number dependence for wavelengths below $\lambda_x/\delta \approx 2\pi$.[19] Encouraged by this result, we apply a $\Delta x/\delta = \pm 4\pi$ window to the correlations of all our channels with box lengths $8\pi\delta$. The result is in Fig. 7(d), and recovers the trend in Fig. 3(e) to longer correlations at higher Reynolds number. Note that we have added to this figure a channel with $\delta^+ = 4200$ and box length $L_x = 2\pi\delta$, for completeness. It follows the same trend as the other three Reynolds numbers, although it should be emphasized that the experiments in Fig. 7(c) do not necessarily imply that its correlations can be trusted in this wider window.

C. Three-dimensional geometric properties

We have already mentioned that distances measured at $y = y'$ do not necessarily represent the correlation dimensions, because the structures are inclined with respect to the wall. The three-dimensional geometry of the correlations is discussed in this section using a variety of measures. The largest dimensions along the three coordinate axes are defined in Fig. 8 as the limits of the bounding box of the correlation contour being considered, measured with respect to the reference correlation point. For example, L_x^u and L_x^d are the maximum distances upstream and downstream of the center, and the maximum correlation length discussed in Sec. III A is $L_x^m = L_x^u + L_x^d$.

The results for C_{uu} are shown in Fig. 9, where the upper row contains channels, and the lower one boundary layers. Shaded regions and line contours correspond to high and low Reynolds numbers, respectively. Note that the left (upstream) half of Figs. 9(a) and 9(d) should be compared with the left (streamwise) half of Figs. 5(a) and 5(d), while each (symmetric) half of Figs. 9(c) and 9(e) should be compared with the right (spanwise) half of Figs. 5(a) and 5(d).

The large-scale features of u are also shorter in boundary layers than in channels in this representation, putting to rest one of the possible reasons for why boundary layers might have been found to be shorter than channels at $y = y'$, which would be that their downstream growth makes their structures more inclined with respect to the wall. We saw in Sec. III A that the total correlation length of the attached structures should be relatively constant across their height, although their position with respect to the central reference point may change. That is indeed the case for $C_{uu} = 0.1$ between $y'/\delta = 0.2$–0.8 in Fig. 9(a), where $L_x^m/\delta \approx 10$ for CH2000 and $L_x^m/\delta \approx 8$ for CH950. As we move away from the wall, L_x^u increases and L_x^d decreases, but in such a way that L_x^m remains roughly constant. That this behavior is connected with the vertical coherence of the global modes[19] can be seen more clearly in Fig. 9(b), which reveals that $C_{uu} = 0.1$ entirely fills the lower half of the channel within that range of y'. The same is true for boundary layers in Fig. 9(e), at least below $y'/\delta = 0.5$. As briefly discussed at the end of Sec. III A, this large vertical dimension provides

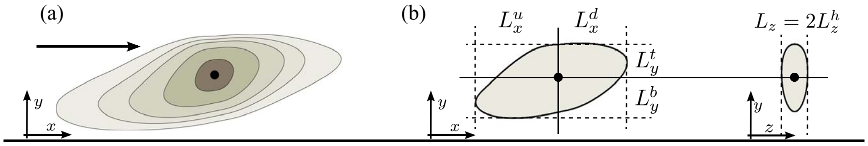

FIG. 8. Sketch of the three-dimensional geometrical properties of the isocontours of given correlation function. (a) Streamwise (xy) section of C_{uu}. The flow is in the direction of the arrow. (b) Dimensions of the bounding box of a given correlation threshold. ●, Reference correlation point.

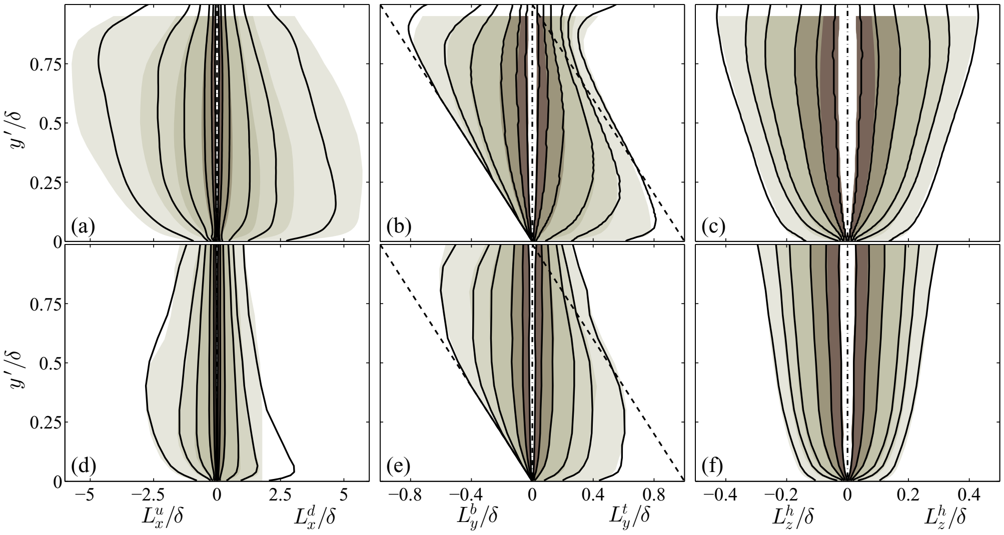

FIG. 9. Three-dimensional maximum correlation size for C_{uu} along the streamwise (a) and (d), wall-normal (b) and (e), and spanwise (c) and (f) directions for channels (top) and boundary layers (bottom). The contours are (0.1,0.2,0.3:0.2:0.9). For all the panels, the shaded contours are CH2000 and *BL*6600 at $\delta^+ \approx 2000$, and solid lines are CH950 and *BL*6600 at $\delta^+ \approx 1300$. The dashed lines in (b) and (e) mark the positions of the wall, y=0, and of y=δ.

a direct link between the wall and the intermittent outer part of the boundary layer. Note that the scaling of L_y with δ is very good, and CH950 falls right on top of CH2000.

Note also that the lengths in Fig. 9 are generally larger than the $y = y'$ ones in Figs. 5(a) and 5(d), and are distributed differently. While the upstream length of C_{uu} peaks around $y'/\delta = 0.5$ in Fig. 5(a), it keeps growing up to $y'/\delta = 0.75$ in Fig. 9(a). Similar differences occur for the boundary layers in Figs. 5(d) and 9(d). The effect is less marked for the spanwise widths, because the structures are not inclined in that direction.

As the correlation threshold increases, the coherence length decreases, and the contribution of the large-scale global modes weakens. For instance, at $C_{uu} = 0.25$, L_x^m is no longer independent of y', nor do the u-structures remain correlated across δ.

A more conventional integral length is defined from the correlation function as[78]

$$\Lambda_{j,\psi} = \int C_{\psi\psi}(\mathbf{r}, \mathbf{r}')\, \mathrm{d}r_j. \tag{5}$$

Unfortunately, the interpretation of this definition is not always straightforward. For example, for a one-dimensional homogeneous signal, (5) is proportional to the energy spectrum at zero wavenumber[78] and, for signals with zero large-scale energy component, it vanishes. Even when this is not the case but the correlation is not everywhere positive, different parts of the integral partially cancel, making the physical interpretation of Λ unclear. In other cases the problem is numerical and, if the integration limits in (5) are chosen too wide, or the number of samples is not large enough, the integration of the noisy correlation tails can lead to errors of the same order as the quantity being measured. Several choices for the integration limits have been proposed to avoid these problems, and the accuracy of the different methods depends on the particular case being considered.[79] For example, it is common to limit the integration to within the first zeros of the correlation function, if they exist, or to the closest intersections with $C = 0.05$. We have adopted this last convention, with the modification that the integral in the wall-normal direction is also truncated to at most $y = \delta$, to avoid the irrotational region in boundary layers. A consequence of this choice is that Λ does not reflect a property of the correlation as a whole, but only of its central positive peak, and tends to track the behavior of the one-dimensional intersections in Fig. 5. On the other hand, since similar procedures are often used in experiments, it is easier to find existing data with which to compare.

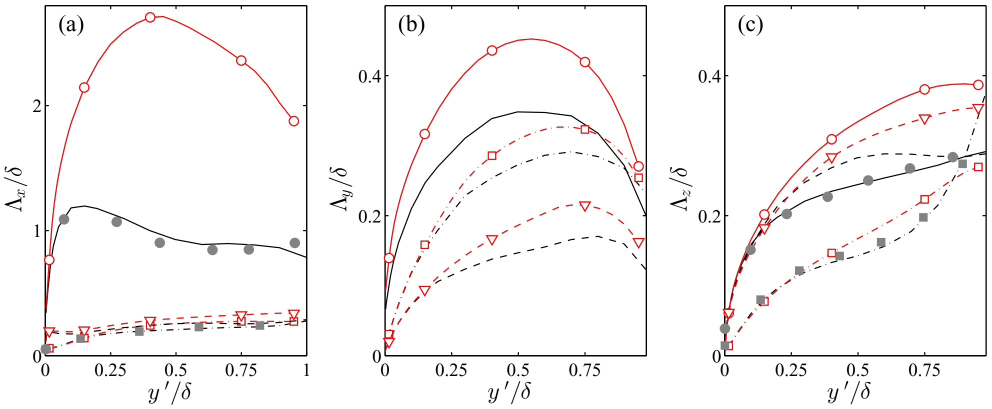

FIG. 10. Integral lengths for boundary layers and channels at $\delta^+ \approx 2000$. (a) Λ_x. (b) Λ_y. (c) Λ_z. For all the panels: —— and ○, u; —·— and □, v; - - - - and ▽, w. Lines without symbols (black) are the present boundary layer, those with open symbols (red) are channels, and closed symbols (gray) are for the compressible boundary layer in Ref. 28.

This is done in Fig. 10, which presents integral lengths for the three velocity components as functions of height. It also includes data from the low-Mach-number boundary layer in Ref. 28, with good agreement.

The difference between $\Lambda_{x,u}$ in boundary layers and channels is again obvious in Fig. 10(a). The integral length grows very fast in both cases across the buffer layer, but it stops growing around $y'/\delta \approx 0.2$ in the boundary layer,[23,26,28,32] and keeps increasing up to $y'/\delta \approx 0.5$ in the channel, mimicking the behavior in Figs. 5(a) and 5(d). What Fig. 10(a) suggests is that the main difference between the two flows is a large-scale structure of u, filling the whole flow thickness and peaking around $y'/\delta \approx 0.5$, which is present in the channels but not in the boundary layers, presumably because the outer-flow intermittency prevents it from forming in the latter. This is probably related to the often quoted observation that the wake component in channels is much weaker than in boundary layers, and that the logarithmic velocity profile extends deeper into the outer region of the former.[22,26] It has been hypothesized that the reason why the correlation length in channels also begins to decrease around $y'/\delta \approx 0.5$ is that the ejections from the opposite wall act as a weaker version of the irrotational inrushes from the free stream.[26,80] That explanation would be consistent with the higher location in Fig. 10(a) of the length maximum in channels than in boundary layers.

The wall-normal and spanwise integral lengths in Figs. 10(b) and 10(c) broadly confirm the behavior of the sections in Fig. 5, but it is interesting to note that Fig. 10(b) illustrates some of the limitations mentioned above for Λ. For example, all the Λ_y decrease above $y'/\delta \approx 0.5$, but mainly because their integral is only taken up to $y = \delta$. More seriously, $\Lambda_{y,w}$ increases linearly away from the wall in the logarithmic region, suggesting self-similarly, but it is always very narrow. Referring back to Figs. 3 and 4, this is seen to be true only for the vertical sections of these structures, and only for its central positive peak. The definition of the integral length fails to capture both the inclination of the correlation and the significance of its negative lobes.

Inspection of the (xy) sections in Fig. 3 shows that any measure of the inclination angle of the correlations depends of the isocontour being considered. A procedure to quantify this dependence is illustrated in Figs. 11(a)–11(c) for CH950. Similar results are obtained for CH2000. Consider a correlation isocontour for a given variable at a given y'. Its (xy) section is generally not elliptical, but it can be approximated by an ellipse having the same second-order tensor of inertia. We do this by assuming that the isocontour bounds a solid shape of constant density, without taking into account the distribution of C within it. The inclination α is defined as the angle between the major semiaxis of that ellipse and the positive x axis. At the same time, the isocontour has a maximum length L_x^m, defined as in Fig. 8. Figures 11(a)–11(c) are maps of both α (shaded contours) and of the isolevels of $C_{\psi\psi}$ used for their computation, drawn as functions of y' and L_x^m for the three velocity components. In general, more intense isocontours have shorter lengths and tend to be more vertical with respect to the wall, probably because the structures become both uncorrelated from their cores and tilted by

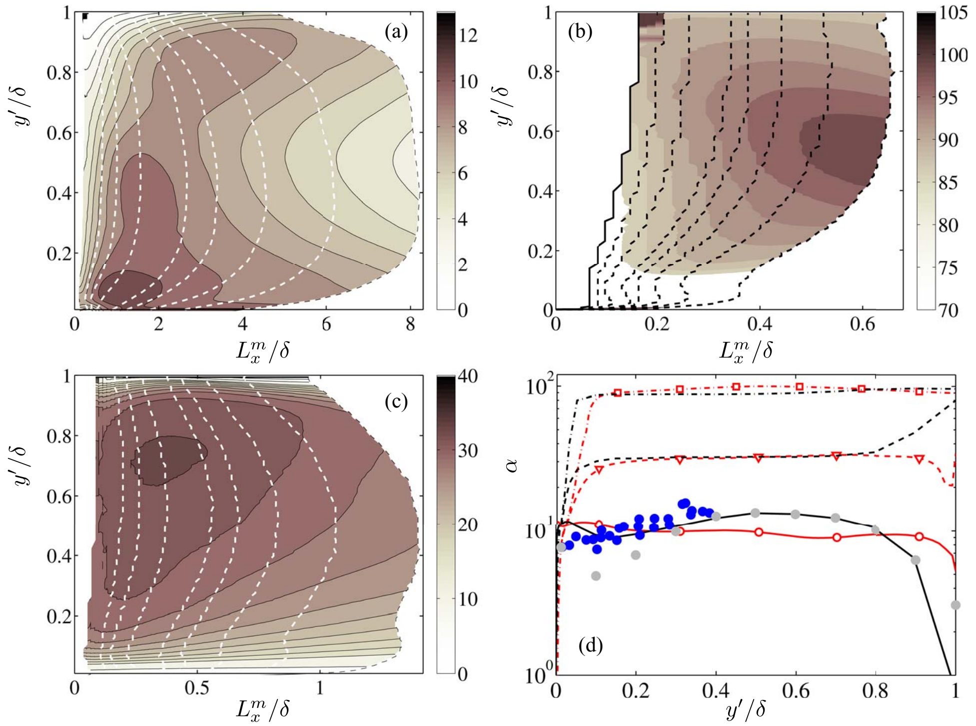

FIG. 11. Inclination angle α for BL6600 at $\delta^+ \approx 2000$, and CH950. (a)–(c) Inclination angle for CH950 as a function of L_x^m/δ and y'/δ for C_{uu}, C_{vv}, and C_{ww}, respectively. Shaded contours are (0:1:13) degrees in (a), (86:2:100) degrees in (b), and (0:5:15 and 17:2:40) degrees in (c). Dashed contours are correlation isolevels (0.1:0.05:0.3 and 0.4, 0.5, 0.6). See text for details. (d) Maximum inclination angle as a function of y'/δ: ——, α_u; —-—, α_v; ----, α_w. Lines without symbols are BL6600, and those with empty symbols (red) are CH950. (gray) is a numerical compressible boundary layer,[28] and (blue) are experimental smooth and rough boundary layers.[43]

the shear as they evolve. A characteristic inclination angle, defined as the maximum angle found at a given height over the range of correlation levels $C \in 0.1$–0.85 (to avoid numerical inaccuracies), is given as a function of y' in Fig. 11(d). It should be borne in mind in interpreting this figure that other inclination angles of the same variable can be defined at the same wall distance, and that the maps in Figs. 11(a)–11(c) are a more complete representation than any single number. Also, inspection of the correlations in Fig. 3 shows that the elliptical model is sometimes only a rough approximation.

Nevertheless, the maximum angles for each velocity component are remarkably uniform across most of the flow, although different from each other. They agree much better between boundary-layers and channels than other measures, probably because, as seen in Figs. 11(a)–11(c), the maximum inclinations correspond to relatively small structures controlled by local, rather than global, processes. Figure 11(d) includes data for α_u from a numerical compressible boundary layer,[28] and from a experimental one including smooth and rough walls.[43] They agree well, especially considering the different flows involved and the slightly different definitions of the inclination angle in each case.

The maximum inclinations for C_{uu} and C_{ww} are achieved for $C \approx 0.3$–0.5, where $\alpha_u \approx 10^\circ$ and $\alpha_w \approx 32^\circ$, respectively. For C_{vv} in Fig. 11(b) there are two regions. Close to the wall, v is blocked by impermeability, and the structures align in the direction of the flow because of the intense shear. In that region, $\alpha_v \approx \alpha_u \approx \alpha_w$. These are the white shaded contours in Fig. 11(b), corresponding to angles $\alpha_v < 75^\circ$. Farther away from the wall, the structures are more inclined, becoming almost vertical, $\alpha_v > 75^\circ$, above $y'^+ \approx 100$. The maximum angle is achieved at $y'/\delta \approx (0.5$–$0.6)$.

The different inclinations of the different variables had been qualitatively noted before,[21] and they are interesting because they seem to contradict the idea of a common structure incorporating the three velocity components. However, this is not necessarily so. Correlations are statistical measures that weight the geometry of a given velocity field with its squared intensity. Thus, any characteristic number extracted from the correlation of some variable most probably represents its geometry when the variable is strongest. Figure 11(d) should therefore be interpreted to mean that u is strongest when the structures are aligned to the streamwise direction, v is strongest when they are normal to the wall, and w is intermediate between the two.[81]

IV. REYNOLDS STRESS CROSS-CORRELATIONS

The cross-correlations of u and v are often used as indications of the structure of the momentum transfer in the form of Reynolds shear stress, $-\langle uv\rangle$,[23,42] although it should be clear that C_{uv} actually expresses the statistical dependence of u at one point on the value of v at another. True momentum transfer is associated with fluctuations at the same location, i.e., $\mathbf{r} = \mathbf{r}'$.

Figures 12(a) and 12(b) present sections of C_{uv} in the near-wall region, $y'^+ \approx 15$, for boundary layers and channels, showing that there is no difference between the two flows at this wall distance. Note that, as in the case of the velocities, continuity constrains the cross-correlations, and

$$\iint R_{uv}\,\mathrm{d}z\,\mathrm{d}y = \iint R_{vu}\,\mathrm{d}x\,\mathrm{d}z = 0. \tag{6}$$

The resulting positive secondary lobes of C_{uv} are clearly seen in Fig. 12(a). If we take their distance to the central point, $\Delta z^+ \approx 50$, as a measure of the width of the stress structure, and the maximum length in Fig. 12(b), $L_x^{m+} \approx 400$, as their streamwise extent or spacing, Figs. 12(a) and 12(b) agree well with the quasi-streamwise vortices of the buffer region.[49]

Interestingly, the minimum (most negative) correlation between u and v in Figs. 12(a) and 12(b) does not occur at zero-distance, but slightly below, at $y^+ \approx 6$ and $x^+ \approx -6$. The stress-structure coefficient derived from one-point statistics is $c_{uv} = -\langle uv\rangle/u'v' \approx 0.40$ at this location, but the maximum value using two-point statistics is 30% higher, $|C_{uv}|_{max} \approx 0.52$. As we move farther from the wall, the difference between the two values decreases. At $y'/\delta \approx 0.8$, $c_{uv} \approx 0.26$ and $|C_{uv}|_{max} \approx 0.32$ in channel flows, and $c_{uv} \approx 0.40$ and $|C_{uv}|_{max} \approx 0.43$ in boundary layers.

The outer-layer correlations in Figs. 12(c) and 12(d) are quite different for boundary layers and channels, reflecting the different dimensions of u in that region. In both cases, C_{uv} is intermediate between C_{uu} and the much shorter C_{vv}. It is interesting that structures connected with the tangential Reynolds stress have lengths of $L_x^m > 1.5\delta$ in boundary layers, and $L_x^m > 2.5\delta$ in channels, even if Fig. 6 shows that there is very little energy in v at those scales. The cospectrum of u and v contains even longer wavelengths extending across the whole flow thickness,[41] corresponding to the global modes mentioned several times in the present paper. These long correlations and spectra have

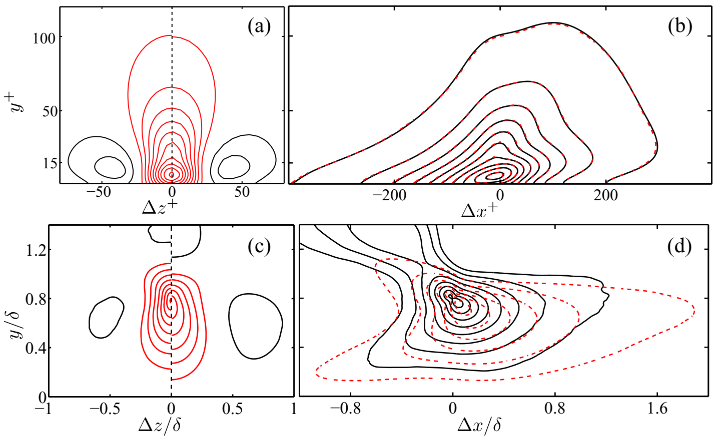

FIG. 12. Contours of C_{uv} at $\delta^+ \approx 2000$ at: (a) and (b) $y'^+ \approx 15$, and (c) and (d) y'/δ=0.8. (a) and (c) Cross-flow (zy) sections. The left half of the figure is the boundary layer, and the right half is the channel. Contours are ±(0.05:0.05:...). Positive contours are black, and negative ones are red. (b) and (d) Streamwise (xy) sections. - - - -, channel (red); ——, boundary layer (black). Contours are (−0.05:−0.05:...). The flow is from left to right.

been interpreted to mean that there are very long structures carrying Reynolds stresses,[26,41,42,46] but Lozano-Durán, Flores, and Jiménez[5] studied the geometry of individual structures of strong uv in channels, and found that they are generally only three times longer than they are high, which is roughly the extent of the correlations in Fig. 12(d). The only exceptions are some extremely long structures, filling most of the channel and roughly as long as the simulation box ($\sim 25\delta$). This agrees with the dimensions of the global modes, but the authors concluded that even these structures are formed by the concatenation of smaller ones of more modest aspect ratio. Closer to the wall, Refs. 82 and 83 analyzed the spatial relation between instantaneous v- and u-structures in the buffer layer of channels, and found that each low-velocity streak is associated with a number of smaller v structures, separated by an average streamwise distance $x^+ \approx 300$.

Liu, Adrian, and Hanratty[42] noted that the cross-correlation of two stochastic variables can be used to generate an optimal basis in which to express the spatial organization of its product, and they used it to discuss the structure of the Reynolds stress. However, the same expansion is not necessarily useful in cases with an underlying deterministic structure. For example, consider a train of pulses of v trailed by another train of pulses of u at a distance $\Delta x = 1$. The cross-correlation C_{uv} has a single maximum at $\Delta x = 1$, but the Reynolds stress is identically zero, because u and v never coincide. In fact, C_{uv} in our flows (Fig. 12) looks like a shorter version of the C_{uu} sections in Sec. III A, while C_{vu} (not shown) looks like a longer version of C_{vv}. The best interpretation is that they represent the extent of the segments of the streamwise-velocity streaks associated with a single sweep or ejection of v. In the different context of autocorrelation functions, Hutchins and Marusic[29] also noted that spectra and correlations are not necessarily good guides to the full length of individual structures.

V. PRESSURE CORRELATIONS

Pressure fluctuations are of interest in engineering because they contribute to noise, vibrations, and material fatigue. They are also the main energy redistribution mechanism among the different velocity components,[36] and are therefore important in the formulation of turbulence models. However, our knowledge about them has improved more slowly than for others flow quantities, also because of the technical difficulties in measuring them, and partly because the global character of pressure requires the consideration of relatively large regions of the flow. Fortunately, DNS data are beginning to change this situation.[18,21,56,58,84]

Here we discuss the three-dimensional two-point spatial correlations of the pressure, C_{pp}, for the simulations in Table I. The pressure is computed from its Poisson equation, using the procedure in Ref. 84 for channels, and the one in Ref. 62 for boundary layers.

Figure 13 is a three-dimensional representation of C_{pp} for the boundary layer, centered at $y'/\delta = 0.6$ and $\delta(x')^+ = 1530$. The domain in the figure is $3\delta \times 1.2\delta \times 4\delta$ in the streamwise, wall-normal, and spanwise direction, representing the central part of the full correlation box. The positive correlation peak is a tall wall-normal structure, moderately elongated in the spanwise direction. Its wall-parallel section through the origin is elliptical, with major axes $a_x \approx 0.75\delta$ and $a_z \approx 1.8\delta$ for $C_{pp} = 0.1$. Its negatively correlated lobes are at $\Delta x \approx \pm\delta$, upstream and downstream of the center, reminiscent of C_{vv} far from the wall (Fig. 6(d)).

A. Lower-dimensional sections

Figure 14 displays two-dimensional cross-flow sections of C_{pp} at three representative locations: the wall, $y' = 0$; the logarithmic layer at $y' = 0.1\delta$; and the outer region at $y' = 0.8\delta$. The representation is the same used in Fig. 4 for the velocity correlations; the left half of each panel is the boundary layer, and the right half is the channel. The figure reveals that the larger scales of the pressure, represented by the weaker correlation contours, are of size $\mathcal{O}(\delta)$ and extend across the whole flow thickness.

Figure 15 contains wall-parallel sections through $y = y'$, at the same streamwise stations as in Fig. 14. It shows that, in spite of the global nature of the pressure fluctuations, very localized regions of strongly coupled structures are found near the reference point, especially as we approach the wall. This agrees with the analysis in Ref. 22, which concluded from the pressure spectra in channels that

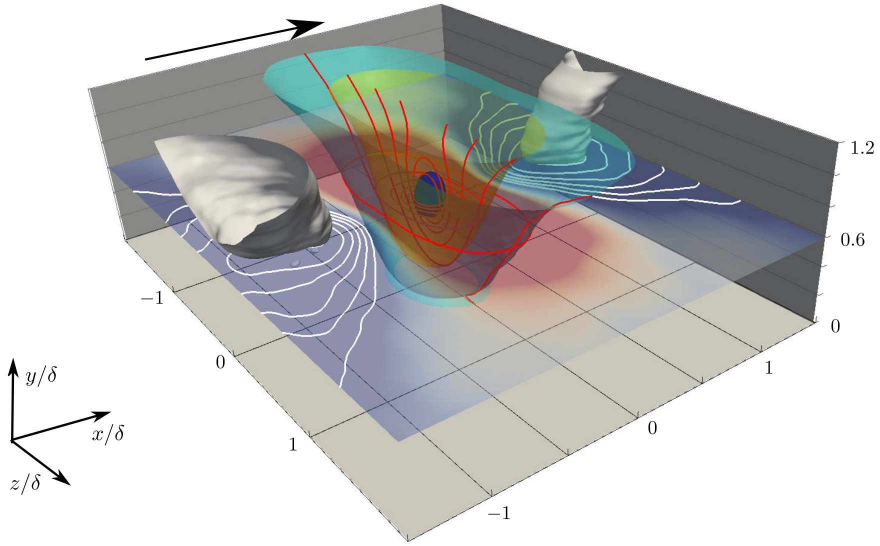

FIG. 13. Three-dimensional correlation of the pressure fluctuations, C_{pp}, for BL6600 at $\delta^+ = 1530$ and $y'/\delta = 0.6$. The flow is from left to right. Several isosurfaces are shown at $C_{pp} = -0.06$ (white), $+0.1$ (turquoise), $+0.2$ (yellow), and $+0.6$ (blue). In the plane sections through the correlation origin, the contour lines of positive and negative correlations are colored red and white, respectively, ranging from 0.1 to 1.0 and from -0.01 to -0.06. The plane sections are also colored by the correlation, ranging from positive red near the center to negative blue at the two streamwise ends of the figure. White is zero.

the structures of p contain a small-scale local component due to velocity structures of the order of the Kolmogorov scales, and a more global one, of size $\mathcal{O}(\delta)$ in the three coordinate directions. The same is true for the correlations. The strongly correlated structures become more localized as the wall is approached, but the weaker contours vary only slowly with y'. Both ranges of contours are relatively isotropic. In particular, note that the weak correlations contours ($C_{pp} < 0.2$) in Figs. 14(a) and 14(b) and Figs. 15(a) and 15(b) are almost identical at the wall and in the logarithmic layer, suggesting that they represent the same wall-attached structure. At this distance from the wall, the small-scale structure of the pressure correlation is very similar in boundary layers and channels, but the larger-scale weaker contours are not, supporting the dual character of the pressure, with small local scales and large global ones. A lower-Reynolds-number case is included for the boundary layer in Figs. 14 and 15. The collapse of the correlation contours is generally poor, probably because the global effects mix contributions from the whole range of scales.

In the outer-layer Fig. 14(c), the pressure remains attached to the wall. In boundary layers, these outer correlations extend all the way from the wall to the potential region. In channels, they reach across the full half-channel, but not to the opposite wall.

Further insight into the structure of the pressure is provided by the one-dimensional sections of C_{pp} in Fig. 16. They are displayed in the same format as the velocities in Fig. 5. The left half

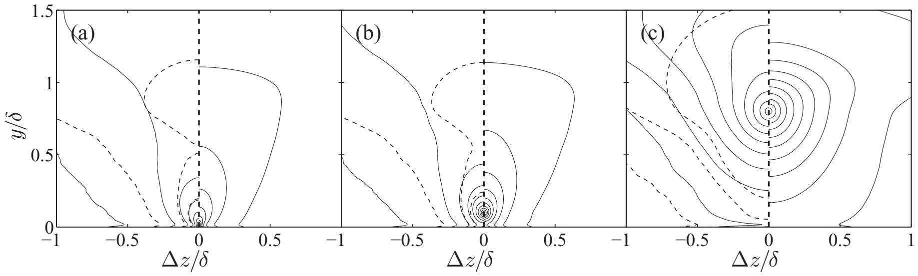

FIG. 14. Cross-flow (zy) sections of C_{pp}. (a) $y' = 0$. (b) $y'/\delta = 0.1$. (c) $y'/\delta = 0.8$. In each panel, the left half is BL6600, and the right half is CH2000. ——, $\delta^+ \approx 2000$; - - - -, $\delta^+ \approx 1313$. Contour levels are (0.05:0.1:0.95).

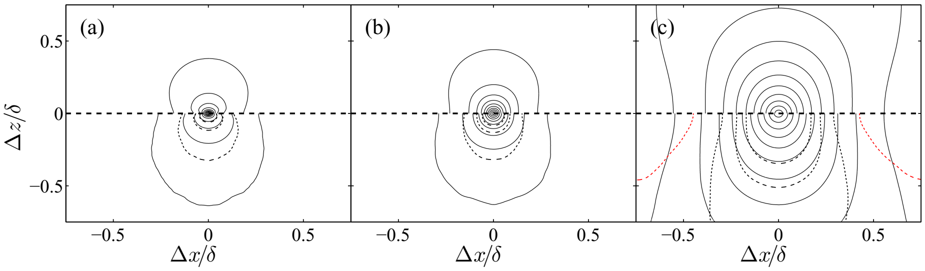

FIG. 15. Wall-parallel (xz) sections of C_{pp}, as in Fig. 14. In each panel, top is CH2000 and bottom is BL6600. The outermost red dashed negative contour in (c) is $C_{pp} = -0.05$.

of each panel contains upstream streamwise sections, and the right half contains spanwise sections as a function of y'. The two panels are for the boundary layer and the channel at roughly the same Reynolds numbers. The boundary layer is both slightly longer and quite wider than the channel. The negative lobe of the streamwise correlation is also deeper in the boundary layer than in the channel, and extends farther from the wall, most probably due to the stronger pressure fluctuations in the potential flow outside the former.[21] In both cases, the length and width of the correlations increases approximately linearly away from the wall, although we saw above that this is mostly due to the intense cores of the correlations. The weaker outer contours are relatively independent of the reference height y', as seen in part by the location of the gap between positive and negative contours in Fig. 16. In fact, their dependence on y' is exaggerated in Fig. 16. We already mentioned in Sec. III A that one-dimensional sections at $y = y'$ give only an incomplete view of the three-dimensional correlations, and it is clear from Fig. 14 that most of the apparent growth of the spanwise correlations in Fig. 16 is because they represent the intersections of similar objects at different heights.

The integral correlations lengths obtained from the one-dimensional sections of C_{pp} are given in Fig. 17, computed as in Sec. III C. There are only minor differences between boundary layers and channels for $\Lambda_{x,p}$ and $\Lambda_{y,p}$, as could be expected from Fig. 16. The streamwise correlation length increases almost linearly with the wall distance. The wall-normal correlation length, $L_{y,p}$, also increases up to $y'/\delta \approx 0.4$, but stabilizes and later decreases above that height. As explained in Sec. III C, this is an artifact of the truncation of the integral (5) to $y \leq \delta$. Note that neither correlation length vanishes at the wall, emphasizing the attached nature of the pressure structures.

The major difference between the pressure correlations of boundary layers and channels in Fig. 16 is their spanwise width, which is almost twice wider for the boundary layer. However, it is unclear whether that result is reliable. The spanwise integral length is not given in Fig. 17 because it was found that the simulation box is too narrow to allow C_{pp} to fully decay at the edge of the box. Note that, because boundary layers grow downstream, their aspect ratio decreases as the Reynolds

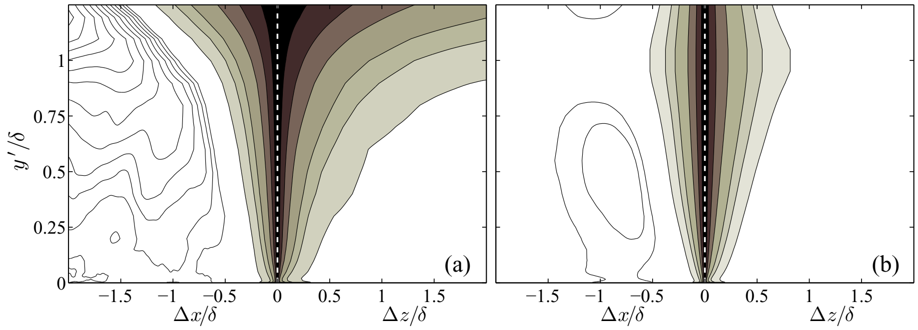

FIG. 16. Single-height ($y = y'$) sections of C_{pp}, as functions of y'/δ. (a) BL6600, $\delta^+ \approx 2000$. (b) CH2000. The left half of each panel is the upstream streamwise section ($\Delta z = 0$). The right half is the spanwise section ($\Delta x = 0$). For all panels, the shaded contours are positive, (0.1,0.2, 0.3:0.2:0.9), and the line contours are negative, (−0.01:−0.01:...).

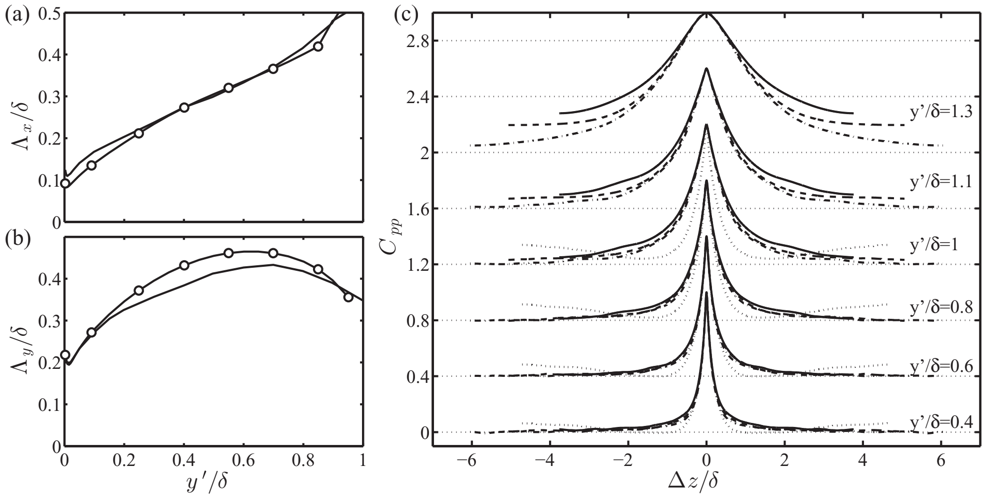

FIG. 17. (a) and (b) Integral correlation lengths for C_{pp} as a function of y'/δ. Lines without symbols are BL6600 at $\delta^+ \approx 2000$; with symbols are CH2000. (a) $\Lambda_{x,p}$. (b) $\Lambda_{y,p}$. (c) Effect of the width of the computational box L_z/δ on the one-dimensional pressure correlation, $C_{pp}(\Delta x = 0, y = y', \Delta z)$ at different heights. Three stations of the boundary layer are presented: —-—, $\delta^+ = 1313$; ----, $\delta^+ = 1530$; ——, $\delta^+ = 1990$. ··········, CH2000. Correlations are offset vertically by 0.4, for clarity.

number increases. In our case, based on previous experience with the velocity correlation in channels, the simulation was dimensioned so that $L_z/\delta \approx 8$ at the downstream end of the simulation box. The actual values for three Reynolds numbers representative of the simulation range, $\delta^+(x') = 1313$, 1530, and 1990, are $L_z/\delta \approx 12$, 10, and 7.5, respectively.

Those three Reynolds numbers are used in Fig. 17(c) as surrogates for the effect of the aspect ratio on the one-dimensional $C_{pp}(\Delta z)$. No major Reynolds-number effects are found for $y'/\delta < 0.8$ but beyond that limit the most downstream station begins to diverge from the other two, and the differences become obvious once we move into the potential region. As already discussed for the velocity correlations, C_{pp} must grow rapidly in size along the potential region to reflect the organization of the large-scale irrotational motions.[54] For example, at $y'/\delta = 0.4$, the values of the correlation at the edge of the box are $C_{pp}(\Delta z = L_z/2) = 0.0016, 0.005$, and 0.02 for the three boundary layer stations mentioned above. The corresponding values at $y'/\delta = 1.3$ are $C_{pp}(L_z/2) = 0.05, 0.2$, and 0.28. It was already known from the pressure spectra in channels that the simulation box of CH2000 ($L_z = 3\pi$) is not wide enough to represent the pressure correctly.[22] Even if it is clear from Fig. 17(c) that the pressure correlations in channels are narrower than in boundary layers, $C_{pp}(L_z/2) = 0.14$ at the centerline of CH2000.

It is a fair question whether these unresolved long-range pressure correlations have an influence on the accuracy of the simulations, and the most likely answer is that they do. The incompressible Navier–Stokes equations only contain pressure gradients, but it was argued in Ref. 22 that they are equations for the accelerations, and that velocity differences correspond to pressure fluctuations. If we take $\Delta p \sim \Delta(u^2)$, the relative uncertainties given above for the pressure correspond to twice the relative uncertainties in the velocities.

VI. CONDITIONAL VELOCITY CORRELATIONS

The correlation $C_{\psi\phi}$ describes the mean value of $\psi(\mathbf{r})$ conditioned to that of $\phi(\mathbf{r}')$ but, because it is an average, it retains no information about the functional relation between the two variables. If that relation is assumed to be linear, Linear Stochastic Estimation (LSE)[16] provides a best estimate for $\psi(\mathbf{r})$ in terms of $\phi(\mathbf{r}')$, but nonlinear relations require higher-order estimates, or conditional statistics.

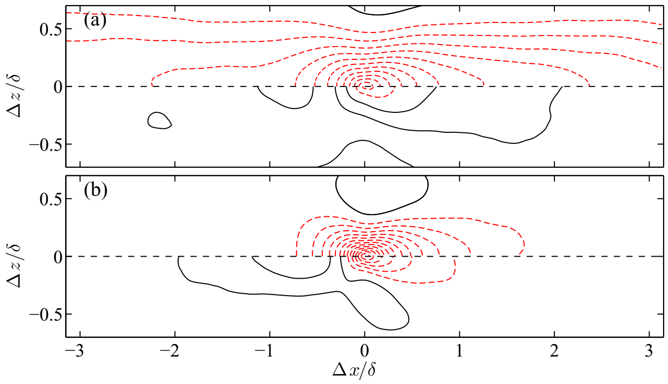

FIG. 18. Wall-parallel (*xz*) sections of the conditional correlation $C_{uv}|_v$ at $y'/\delta = 0.6$ and $\Gamma = 0$. (a) CH2000. (b) BL6600 at $\delta^+ \approx 1530$. For all the panels: correlations conditioned to positive events $C^{\oplus}_{uv}|_v$ are shown at the top half, and those conditioned to negative events $C^{\ominus}_{uv}|_v$, on the bottom. See text for details. Contours are ±(0.02:0.03:...). ——, positive; - - - -, negative.

Define the conditional correlations,

$$C^{\oplus}_{\psi\phi}(\mathbf{r},\mathbf{r}')|_{\xi} = \frac{\langle \psi(\mathbf{r})\cdot\phi(\mathbf{r}')\rangle|_{\xi(\mathbf{r}')>\Gamma}}{\sigma_{\psi}(\mathbf{r})\cdot\sigma_{\phi}(\mathbf{r}')|_{\xi(\mathbf{r}')>\Gamma}} \quad \text{and} \quad C^{\ominus}_{\psi\phi}(\mathbf{r},\mathbf{r}')|_{\xi} = \frac{\langle \psi(\mathbf{r})\cdot\phi(\mathbf{r}')\rangle|_{\xi(\mathbf{r}')<-\Gamma}}{\sigma_{\psi}(\mathbf{r})\cdot\sigma_{\phi}(\mathbf{r}')|_{\xi(\mathbf{r}')<-\Gamma}}, \tag{7}$$

where the three variables involved are not necessarily the same, and the condition is that $\xi(\mathbf{r}')$ has to be stronger than a given threshold, $\pm\Gamma$, typically chosen as a fraction of the standard deviation $\sigma_{\xi}(y')$. When $\Gamma = 0$, the two correlations separate positive from negative events.

Consider first the conditional cross-correlations $C_{uv}|_v$ in a wall-parallel (*xz*) section at $y'/\delta = 0.6$, presented in Fig. 18. The top half of each panel is conditioned to positive $v > 0$ (outwards motions), whereas the lower half is conditioned to $v < 0$ (inwards motions). Using the classical quadrant analysis terminology,[85,86] most of the inwards motions correspond to Q2 ejections ($v > 0$ and $u < 0$), whereas to Q4 sweeps ($v < 0$ and $u > 0$) for the inwards motions case. Fig. 18(a) shows that the ejections, that typically correspond to low-speed streaks, are considerably longer in channels than the sweeps. This agrees with the analysis of Lozano-Durán, Flores, and Jiménez,[5] who extracted individual structures of strong $-\langle uv\rangle$ in channels, and found that, although Q2s and Q4s were of comparable size throughout the inner and logarithmic layer, the ejections became much longer than the sweeps farther from the wall. Both conditional correlations in Fig. 18(a) are biased downstream from the reference point, showing that the wall-normal velocity events are predominantly located near the front of the streaks.[82] Fig. 18(b) repeats the analysis for the boundary layer, and shows that the lengths of the two types of streaks are closer to each other than in channels. This is especially true for the outwards events, strongly suggesting that the differences discussed in Sec. III between the lengths of C_{uu} in both types of flows are mostly due to the low-speed structures of the outer layer. Note that the difference between the conditional correlations of inwards and outwards motions is not unexpected, because the events associated to those quadrants contribute differently to the Reynolds stress depending on the distance to the wall, even at $\mathbf{r} = \mathbf{r}'$. That difference increases in the outer layer,[87] and at $y' = 0.6\delta$ and zero separation the fractional contribution to the Reynolds stress of the outward ($Q1$ and $Q2$) and inward ($Q3$ and $Q4$) events are, respectively, $R^{\oplus}_{uv}|_v/R_{uv} \approx 0.78$ and $R^{\ominus}_{uv}|_v/R_{uv} \approx 0.22$ in the case of the channel flow, and 0.64 and 0.36 in the case of the boundary layer. Note that the value of the denominator in (7) differs little between the two conditional correlations, because the probability distribution of v is roughly symmetric at that height (not shown). Therefore, the differences observed can be attributed first to the weaker inwards motions at the middle of the outer layer, and secondly, to the much longer low-velocity streaks in channel flows.

Lee and Sung[32] recently used the conditional $C_{uu}|_u$ in the wall-parallel sections of a pipe ($\Gamma = 0$) to differentiate between the structure of high- and low-velocity streaks, and found very little difference between the two. Baltzer, Adrian, and Wu[51] repeated their analysis with a slightly more complicated condition, and got similar results for the low-speed streaks. They did not analyze

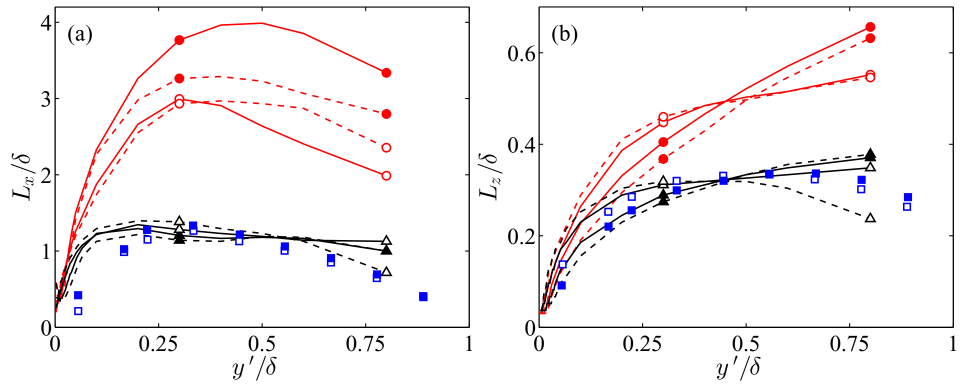

FIG. 19. Length of the conditional correlation, $C_{uu}|_u = 0.3$, as a function of y'/δ. (a) Streamwise. (b) Spanwise. ○ (red), CH2000; △ , BL6600 at $\delta^+ = 1530$; □ (blue), pipe at $\delta^+ = 934$.[32] ——, $\Gamma = 0$; - - - -, $\Gamma = 1.5\sigma_u$. Open symbols are $C^{\oplus}$, and closed ones are $C^{\ominus}$.

in detail the high-speed structures, citing Ref. 32 to justify the assumption they are similar to the low-speed ones. On the other hand, previous visualizations had found that, at least near the wall, low-velocity streaks are longer than high-velocity ones.[13,82] One reason for this discrepancy is probably the conditioning threshold. Both correlation studies used $\Gamma = 0$, while visual analyses[29] or segmentation algorithms[5,17,82,83] usually rely on a higher threshold to separate high from low speed. For example, the streaks in Refs. 82 and 83 were characterized as connected regions in which the streamwise velocity is more than one standard deviation away from its mean ($\Gamma = \sigma_u$). Both papers found that the low-momentum streaks differ most from the high-momentum ones at $y^+ \approx 10$, where they are 85% longer.

The analysis in Ref. 32 is repeated and compared in Fig. 19 for boundary layers and channels, using two different thresholds. It is found that the threshold changes substantially the correlation length, although in different ways for different flows and locations. Most visible in the figure are the changes for the channel away from the wall, where a high threshold tends to make the two conditional signs more equal. Although hard to see in the figure, the opposite is true below $y'^+ = 15$. The low-speed correlations, $C^{\ominus}_{uu}|_u$, are longer in that region than the high-speed ones, and the ratio of the lengths at $y'^+ = 10$ changes from 1.15 at $\Gamma = 0$ to about 1.5 for $\Gamma = 1.5\sigma_u$. However, the largest difference in Fig. 19 is between the channel and the other two flows. Not only is the channel much longer than both the pipe and the boundary layer, in agreement with the results for the unconditional correlation, but it is also the only flow for which low-speed structures are substantially longer than the high-speed ones far from the wall. The widths in Fig. 19(b) have a complicated dependence on y'. In the three flows, high-speed structures are wider than low-speed ones below $y'/\delta \approx 0.5$, and narrower above that level, although the differences are not great.

Another interesting set of correlations are those conditioned on the sign of w, because a consequence of the symmetry of the problem is that correlations would be symmetric in z even if the underlying structures were not. The wall-parallel sections of the unconditional correlations C_{ww}, which were not included in Fig. 6, are presented in Figs. 20(a) and 20(c). They are characteristically squarish, suggesting that they are the superposition of two diagonals, presumably associated with the sign of w. This is confirmed by Figs. 20(b) and 20(d), which present $C^{\oplus}_{ww}|_w$. Both for the channel and for the boundary layer, the conditional correlations are aligned to the 45° diagonal, most clearly so for the boundary layer. By symmetry, $C^{\ominus}_{ww}|_w$ is aligned to the opposite diagonal, and is not shown. The effect is stronger far from the wall. The shaded contours that correspond to $y'/\delta = 0.1$ in Figs. 20(b) and 20(d) are actually slightly inclined in the opposite direction to those away from the wall. Since we saw in Fig. 4 that w is an attached variable in which the correlation of the large outer scales changes sign near the wall, this negative inclination is probably due to that counterflow. The dimensions of the near-wall correlations in Fig. 20, which are comparable to those away from the wall, support this interpretation.

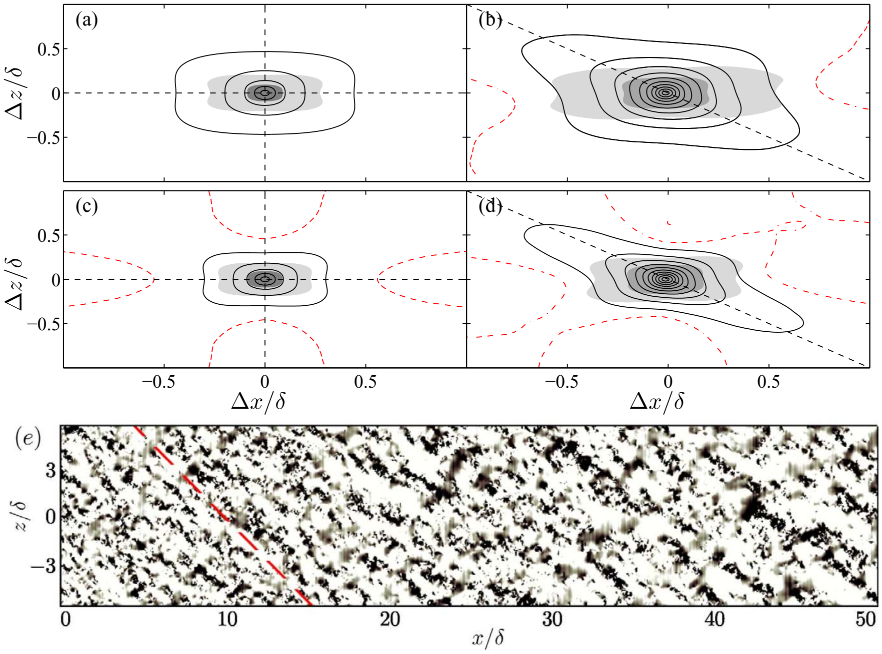

FIG. 20. Wall-parallel (xz) sections of the correlation of the spanwise velocity at $y'/\delta = 0.1$ (shaded) and $y'/\delta = 0.8$ (lines). (a) and (b) CH2000. (c) and (d) BL6600 at $\delta^+ \approx 1530$. (a) and (c) Unconditional correlations. Positive contours (black solid lines) are C_{ww}=(0.1:0.2:...). Negative contours (red dashed lines) are $C_{ww} = -(0.02{:}0.1{:}\ldots)$. The shaded contours are $C_{ww} = 0.1, 0.3$. (b) and (d) Conditioned to $w > 0$, $C^{\oplus}_{ww}|_w$. Contours are twice smaller than in (a) and (c). The dashed diagonal is inclined at 45° to the mean velocity. (e) Instantaneous plane of w at $y = \delta(x)$ and $Re_\theta = 3040$–5870 ($\delta^+ \approx 1050$–1810). The axes are normalized with the thickness δ taken at the middle of the box, $Re_\theta = 4500$, and w with the x-dependent friction velocity. Dark areas are $0 < w < 1.5\sigma_w$. Dashed line as in (b).

The diagonal alignment of the structures of w is surprising, and strong enough to be seen in instantaneous flow fields (Fig. 20(e)). Its scale is also large enough for visible stripes to cross the whole spanwise simulation domain, $\sim 10\delta$. Weak diagonal structures of roughly similar orientation have been reported in smoke visualizations of a boundary layer at very low Reynolds numbers.[88] Baltzer, Adrian, and Wu[51] isolated helical features of u in a pipe by separating Fourier modes with different helicities, but their inclination with respect to x was only ∼5°, much shallower than those found here. These researchers were motivated by the "hourglass" shape of the unconditional correlation C_{uu}, which is also visible in Fig. 6(a) and 6(c) above. Hutchins and Marusic,[29] while studying the meandering of the logarithmic-layer streaks of u in boundary layers, had noted that such correlations were likely to correspond to the superposition of two independent diagonal structures. The square shape of C_{ww} in Figs. 20(a) and 20(c) is an extreme example of that phenomenon, but

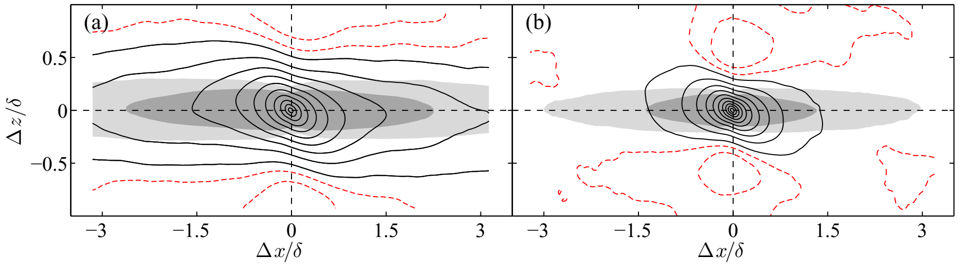

FIG. 21. Wall-parallel (xz) sections of the conditional correlation $C_{uu}|_w$ with $w(\mathbf{r}') > 1.5\sigma_w$. (a) CH2000. (b) BL6600 at $\delta^+ \approx 1530$. Lines and contours as in Fig. 20(b).

note that we do not separate the two orientations by selecting inclined Fourier modes, but by the sign of the conditioning spanwise velocity. In fact, it can be shown that the diagonal structure is associated with relatively strong w. The elongated shape of the conditional correlation is accentuated when the threshold is chosen as $w(\mathbf{r}') > 1.5\sigma_w$. It becomes more circular when only considering weak conditioning velocities, $|w(\mathbf{r}')| < 1.5\sigma_w$, but it never completely disappears. We cannot offer at the moment an explanation for this structure, but it is interesting that it is also present in channels, where it appears to be contaminated by the opposite orientation of a similar structure coming from the other half of the channel. In boundary layers, it is a property of the rotational turbulent flow. It cannot be found beyond $y'/\delta = 1.05$.

That the spanwise velocity is also able to distort u is tested by the conditional correlations $C_{uu}|_w$ in Fig. 21. The skew is now only $\sim 7^\circ$, closer to that in Ref. 51, and probably corresponds to the meandering discussed in Ref. 29. It can only be clearly seen when conditioning by relatively strong velocities, $\Gamma = 1.5\sigma_w$, but it suggests that the meandering of u is a consequence of the more obvious diagonal organization of w.

VII. SUMMARY AND CONCLUSIONS

Fully three-dimensional two-point statistics of a new zero-pressure-gradient turbulent boundary layer[18] up to $Re_\theta \approx 6600$ ($\delta^+ \approx 2000$) have been presented and compared with turbulent channels at similar Reynolds numbers. We considered very large domains $\mathcal{O}(20\delta)$ to observe the largest scales present in the flow and to educe the average spatial structure of the velocity and pressure fluctuations in the buffer, logarithmic, and outer regions.

We have shown that the streamwise-velocity correlations are coherent over longer distances in channels than in boundary layers, especially in the direction of the flow. Along that direction, the maximum length of the weakly correlated structures is $\mathcal{O}(18\delta)$ in channels and $\mathcal{O}(7\delta)$ in boundary layers, attained within the outer and logarithmic layers, respectively. We argue that those correlation lengths do not change significantly from the near-wall to the outer region because they essentially reflect different aspects of a common large-scale structure, implying that the energy from the larger outer structures reaches the neighborhood of the wall. The behavior of the integral correlation lengths along the streamwise direction suggests that the main difference between the two flows is a large-scale structure that fills the whole flow thickness and peaks around $y' \approx 0.5\delta$. That structure is only present in channels, most likely because the intermittent character of the edge of the boundary layer prevents its growth. We have linked these very large structures with the global modes identified by del Álamo *et al.*,[19] whose intensity fails to scale either in outer or in wall units. Such large scales are absent in the spanwise and wall-normal velocity components, whose maximum streamwise lengths, $\mathcal{O}(\delta\text{–}2\delta)$, change little with the type of flow and with the Reynolds number. On the other hand, the three velocity components have similar spanwise widths, $\mathcal{O}(\delta)$. The correlations are shown to be inclined to the wall with different angles that depend on the distance to the wall and on the correlation level used to define them. Despite that, the maximum angle for each velocity component is remarkably uniform across most of the flow, differing little between channels and boundary layers. That is explained because those angles are associated with smaller structures that are probably controlled by local processes rather than by global ones. The maximum inclination angle of the velocity structures is $\alpha_u \approx 10^\circ$ for the streamwise velocity and $\alpha_w \approx 32^\circ$ for the spanwise velocity, whereas C_{vv} is essentially vertical. We have noted that these different inclinations probably reflect the moments in the evolution of the structures at which each velocity component is most intense.

The functional form of the velocity correlations is not arbitrary, because incompressibility requires that the correlation flux over any plane normal to a given velocity component has to vanish.[14] This cancellation is reflected in the cross-flow (zy) plane of C_{uu} as low- and high-momentum streaks organized at δ-scale, and in the streamwise (xy) plane of C_{ww} as alternating thin layers stacked in the wall-normal direction. However, the return flow in the wall-parallel (xz) plane of C_{vv} is not as clear, and is organized as a central compact down(up)-wash surrounded by a more diffuse counter-flow. This flow configuration suggests that channels and boundary layers organize themselves into inclined quasi-streamwise rollers of size $\mathcal{O}(\delta)$, at least within the logarithmic layer and the inner part of the outer region. Two transitions take place beyond the middle of the outer region in boundary layers, but are either absent or weaker in channel flows. The first transition is at $y' \approx 0.6\delta$, where the negative lobes of C_{vv} switch from a spanwise side-to-side configuration to an upstream-downstream one, whereas in channels an incomplete version of that switch occurs at $y' \approx 0.8\delta$. The second transition is exclusive of boundary layers and is located at its edge, $y' \approx \delta$, where all the correlations grow rapidly in size to reflect the larger irrotational structures of the free stream. Similarly to C_{vv}, the spanwise negative lobes of C_{uu} are replaced by streamwise ones, suggesting that the flow is organized in that region as a more isotropic or spanwise-oriented configuration, rather than as a streamwise-oriented one.

We have studied the cross-correlation C_{uv} for the Reynolds shear stress, and argued that it should be interpreted as reflecting the dimensions of the segments of the streamwise-velocity streaks associated with a single sweep or ejection of v, rather than the organization of the true momentum transfer. The latter is exclusively associated to fluctuations of u and v at a common location. At $y'^+ \approx 15$ there are no differences between boundary layers and channels, whereas they differ considerably in the outer layer, probably because of the corresponding differences in C_{uu}. The length of C_{uv} is intermediate between that of C_{uu} and the much shorter C_{vv}. Its minimum value also differs in magnitude and location from the one-point structure coefficient. The aspect ratios of C_{uv} are roughly similar to those of the instantaneous Reynolds-stress structures studied by Lozano-Durán, Flores, and Jiménez[5] using segmentation algorithms, whose average length is three times their height.

Using spectra, Jiménez and Hoyas[22] concluded that the pressure structures contain a local component at the Kolgomorov scale and a more global one with scales of $\mathcal{O}(\delta)$ along the three coordinate directions. Inspection of C_{pp} at the wall, in the logarithmic layer, and in the outer layer reveals a similar behavior. Weakly correlated structures vary little with y in boundary layers and channels, at least below the outer region, but they differ between the two flows, suggesting that they represent different views of a single large-scale structure that is different for each flow. On the contrary, strongly correlated structures are similar in both flows, but vary with y, emphasizing the local character of the small-scale pressure. The weaker contours of C_{pp} collapse poorly with the Reynolds numbers, probably because the global effects mix contributions from all scales. The major difference between the two flows occurs in the spanwise width of C_{pp}, which is almost twice wider for the boundary layer than for the channel. However, it is unclear whether that result is reliable, because the pressure structures above $y' \approx 0.8\delta$ seem to be constrained by the box width in both simulations.

Finally, to further investigate the relations between the different velocity components, we have defined correlations conditioned on the intensity and sign of the perturbations at the reference point. The cross-correlation of C_{uv} conditioned on the sign of v reveals that the ejections in channel flows becomes much longer than the sweeps above the logarithmic layer, whereas that difference is only moderate in boundary layers. That suggest that the differences observed in the length of C_{uu} are mostly due to low-momentum structures in the outer layer, recalling the observation at the beginning of this section that channels contain a large-scale outer structure that is absent from boundary layers. The evolution with y of the correlation length of the low- and high-momentum streaks was computed by considering C_{uu} conditioned on different intensities of the reference fluctuation of u, and compared with the pipe flow simulation of Lee and Sung.[32] We found that channels are the only flow in which the low-momentum structures are substantially longer, when characterized via correlations, than the high-momentum ones far from the wall, whereas the two lengths are similar in pipes and in boundary layers.

The spatial organization of w was shown to be especially interesting. Its striking squarish shape turns out to be the superposition of two diagonal orientations. Conditioning the wall-parallel sections of C_{ww} on the sign of w results in a correlation that is aligned at ±45° to the mean flow in the outer layer, although not near the wall. This correlation is strong enough to be visible in instantaneous flow visualizations of w. Similarly conditioning C_{uu} on intense events of w results in correlations inclined at approximately ±7° with respect to x in the outer region, but not near the wall. This suggests that the meandering of u is a consequence of the spatial organization of w, although further research is needed to clarify the mechanism that leads to that diagonal organization.

ACKNOWLEDGMENTS

This research was funded in part by the Spanish CICYT under Grant No. TRA2009-11498, and by the European Research Council under Grant No. ERC-2010.AdG-20100224. It used the computational resources of the Argonne Leadership Computing Facility at Argonne National Laboratory, which is supported by the Office of Science of the U.S. Department of Energy under Contract No. DE-AC02-06CH11357. J. A. Sillero was supported in part by an FPU fellowship from the Universidad Politécnica de Madrid. We are deeply grateful to A. Gungor for her careful revision of the first version of the manuscript.

[1] A. A. Townsend, "The turbulent boundary layer," in *Boundary Layer Research*, International Union of Theoretical and Applied Mechanics, edited by H. Görtler (Springer, Berlin, 1958), pp. 1–15.
[2] H. L. Grant, "The large eddies of turbulent motion," J. Fluid Mech. **4**, 149–190 (1958).
[3] A. J. Favre, J. J. Gaviglio, and R. Dumas, "Space-time double correlations and spectra in a turbulent boundary layer," J. Fluid Mech. **2**, 313–342 (1957).
[4] S. J. Kline, W. C. Reynolds, F. A. Schraub, and P. W. Runstadler, "The structure of turbulent boundary layers," J. Fluid Mech. **30**, 741–773 (1967).
[5] A. Lozano-Durán, O. Flores, and J. Jiménez, "The three-dimensional structure of momentum transfer in turbulent channels," J. Fluid Mech. **694**, 100–130 (2012).
[6] L. S. G. Kovasznay, V. Kibens, and R. R. Blackwelder, "Large-scale motion in the intermittent region of a turbulent boundary layer," J. Fluid Mech. **41**, 283–325 (1970).
[7] J. Murlis, H. M. Tsai, and P. Bradshaw, "The structure of turbulent boundary layers at low Reynolds numbers," J. Fluid Mech. **122**, 13–56 (1982).
[8] H. P. Bakewell and J. L. Lumley, "Viscous sublayer and adjacent wall region in turbulent pipe flow," Phys. Fluids **10**, 1880–1889 (1967).
[9] E. R. Corino and R. S. Brodkey, "A visual investigation of the wall region in turbulent flow," J. Fluid Mech. **37**, 1–30 (1969).
[10] J. Jiménez, "Near-wall turbulence," Phys. Fluids **25**, 101302 (2013).
[11] J. Jiménez, "The largest scales of turbulence," in *CTR Ann. Res. Briefs* (Stanford University, 1998), pp. 137–154.
[12] K. Kim and R. J. Adrian, "Very large-scale motion in the outer layer," Phys. Fluids **11**, 417–422 (1999).
[13] S. K. Robinson, "Coherent motions in the turbulent boundary layer," Annu. Rev. Fluid Mech. **23**, 601–639 (1991).
[14] A. A. Townsend, *The Structure of Turbulent Shear Flows*, 2nd ed. (Cambridge University Press, 1976).
[15] A. E. Perry, S. Henbest, and M. S. Chong, "A theoretical and experimental study of wall turbulence," J. Fluid Mech. **119**, 163–199 (1986).
[16] C. D. Tomkins and R. J. Adrian, "Spanwise structure and scale growth in turbulent boundary layers," J. Fluid Mech. **490**, 37–74 (2003).
[17] J. C. del Álamo, J. Jiménez, P. Zandonade, and R. D. Moser, "Self-similar vortex clusters in the turbulent logarithmic region," J. Fluid Mech. **561**, 329–358 (2006).
[18] J. A. Sillero, J. Jiménez, and R. D. Moser, "One-point statistics for turbulent wall-bounded flows at Reynolds numbers up to $\delta^+ \approx 2000$," Phys. Fluids **25**, 105102 (2013).
[19] J. C. del Álamo, J. Jiménez, P. Zandonade, and R. D. Moser, "Scaling of the energy spectra of turbulent channels," J. Fluid Mech. **500**, 135–144 (2004).
[20] S. Hoyas and J. Jiménez, "Scaling of the velocity fluctuations in turbulent channels up to $Re_\tau = 2003$," Phys. Fluids **18**, 011702 (2006).
[21] J. Jiménez, S. Hoyas, M. P. Simens, and Y. Mizuno, "Turbulent boundary layers and channels at moderate Reynolds numbers," J. Fluid Mech. **657**, 335–360 (2010).
[22] J. Jiménez and S. Hoyas, "Turbulent fluctuations above the buffer layer of wall-bounded flows," J. Fluid Mech. **611**, 215–236 (2008).
[23] D. J. Tritton, "Some new correlation measurements in a turbulent boundary layer," J. Fluid Mech. **28**, 439–462 (1967).
[24] G. Comte-Bellot, "Écoulement turbulent entre deux parois parellèles," Pub. Scientifiques Techniques (Ministère de L'Air, 1965), Vol. 419.
[25] A. A. Townsend, "Equilibrium layers and wall turbulence," J. Fluid Mech. **11**, 97–120 (1961).
[26] B. Ganapathisubramani, N. Hutchins, W. T. Hambleton, E. K. Longmire, and I. Marusic, "Investigation of large-scale coherence in a turbulent boundary layer using two-point correlations," J. Fluid Mech. **524**, 57–80 (2005).
[27] J. H. Lee and H. J. Sung, "Very-large-scale motions in a turbulent boundary layer," J. Fluid Mech. **673**, 80–120 (2011).
[28] S. Pirozzoli and M. Bernardini, "Turbulence in supersonic boundary layers at moderate Reynolds number," J. Fluid Mech. **688**, 120–168 (2011).
[29] N. Hutchins and I. Marusic, "Evidence of very long meandering features in the logarithmic region of turbulent boundary layers," J. Fluid Mech. **579**, 467–477 (2007).
[30] K. J. Bullock, R. E. Cooper, and F. H. Abernathy, "Structural similarity in radial correlations and spectra of longitudinal velocity fluctuations in pipe flow," J. Fluid Mech. **88**, 585–608 (1978).
[31] K. T. Christensen, "Experimental investigation of acceleration and velocity fields in turbulent channel flow," Ph.D. thesis, University of Illinois at Urbana-Champaign, 2001.
[32] J. H. Lee and H. J. Sung, "Comparison of very-large-scale motions of turbulent pipe and boundary layer simulations," Phys. Fluids **25**, 045103 (2013).

[33] P. Moin and J. Kim, “Numerical investigation of turbulent channel flow,” J. Fluid Mech. **118**, 341–377 (1982).
[34] J. W. Deardorff, “A numerical study of three-dimensional turbulent channel flow at large Reynolds numbers,” J. Fluid Mech. **41**, 453–480 (1970).
[35] P. Moin and J. Kim, “The structure of the vorticity field in turbulent channel flow. Part 1. Analysis of instantaneous fields and statistical correlations,” J. Fluid Mech. **155**, 441–464 (1985).
[36] H. Tennekes and L. J. Lumley, *First Course in turbulence* (MIT Pres, 1972).
[37] R. J. Adrian, C. D. Meinhart, and C. D. Tomkins, “Vortex organization in the outer region of the turbulent boundary layer,” J. Fluid Mech. **422**, 1–53 (2000).
[38] M. R. Head and P. Bandyopadhyay, “New aspects of turbulent boundary-layer structure,” J. Fluid Mech. **107**, 297–338 (1981).
[39] T. Theodorsen, “Mechanism of turbulence,” in *Proceedings of the Second Midwestern Conference on Fluid Mechanics, Columbus, Ohio, 17–19 March 1952* (The Ohio State University, 1952), pp. 1–19.
[40] J. C. del Álamo and J. Jiménez, “Spectra of the very large anisotropic scales in turbulent channels,” Phys. Fluids **15**, L41–L44 (2003).
[41] J. Jiménez, “Cascades in wall-bounded turbulence,” Annu. Rev. Fluid Mech. **44**, 27–45 (2012).
[42] Z. Liu, R. J. Adrian, and T. J. Hanratty, “Large-scale modes of turbulent channel flow: Transport and structure,” J. Fluid Mech. **448**, 53–80 (2001).
[43] Y. Wu and K. T. Christensen, “Spatial structure of a turbulent boundary layer with irregular surface roughness,” J. Fluid Mech. **655**, 380–418 (2010).
[44] M. Guala, S. E. Hommema, and R. J. Adrian, “Large-scale and very-large-scale motions in turbulent pipe flow,” J. Fluid Mech. **554**, 521–542 (2006).
[45] J. P. Monty, J. A. Stewart, R. C. Williams, and M. S. Chong, “Large-scale features in turbulent pipe and channel flows,” J. Fluid Mech. **589**, 147–156 (2007).
[46] M. Tutkun, W. K. George, J. Delville, M. Stanislas, P. B. V. Johansson, J.-M. Foucaut, and S. Coudert, “Two-point correlations in high Reynolds number flat plate turbulent boundary layers,” J. Turbul. **10**, 21 (2009).
[47] S. C. C. Bailey and A. J. Smits, “Experimental investigation of the structure of large- and very-large-scale motions in turbulent pipe flow,” J. Fluid Mech. **651**, 339–356 (2010).
[48] D. J. C. Dennis and T. B. Nickels, “Experimental measurement of large-scale three-dimensional structures in a turbulent boundary layer. Part 2. Long structures,” J. Fluid Mech. **673**, 218–244 (2011).
[49] J. Kim, P. Moin, and R. D. Moser, “Turbulence statistics in fully developed channel flow at low Reynolds number,” J. Fluid Mech. **177**, 133–166 (1987).
[50] J. H. Lee, J. Lee, and H. J. Sung, “Spatial features of the wall-normal structures in a turbulent boundary layer,” J. Turbul. **12**, N46 (2011).
[51] J. R. Baltzer, R. J. Adrian, and X. Wu, “Structural organization of large and very large scales in turbulent pipe flow simulation,” J. Fluid Mech. **720**, 236–279 (2013).
[52] P. Moin and R. D. Moser, “Characteristic–Eddy decomposition of turbulence in a channel,” J. Fluid Mech. **200**, 471–509 (1989).
[53] M. Tanahashi, S.-J. Kang, T. Miyamoto, S. Shiokawa, and T. Miyauchi, “Scaling law of fine scale eddies in turbulent channel flow at to $Re_\tau = 800$,” Int. J. Heat Fluid Flow **25**, 331–340 (2004).
[54] T. M. Farabee and M. J. Casarella, “Spectral features of wall pressure fluctuations beneath turbulent boundary layers,” Phys. Fluids A **3**, 2410–2420 (1991).
[55] H. Choi and P. Moin, “On the space-time characteristics of wall-pressure fluctuations,” Phys. Fluids A **2**, 1450–1460 (1990).
[56] Z. Hu, C. Morley, and N. Sandham, “Wall pressure and shear stress spectra from direct simulations of channel flow,” AIAA J. **44**, 1541–1549 (2006).
[57] Y. Tsuji, J. H. M. Fransson, P. H. Alfredsson, and A. V. Johansson, “Pressure statistics and their scaling in high-Reynolds-number turbulent boundary layers,” J. Fluid Mech. **585**, 1–40 (2007).
[58] J. Kim, “On the structure of pressure fluctuations in simulated turbulent channel flow,” J. Fluid Mech. **205**, 421–451 (1989).
[59] V. J. Shinde, J.-P. Laval, and M. Stanislas, “Effect of mean pressure gradient on the turbulent wall pressure–velocity correlations,” J. Turbul. **15**, 833–856 (2014).
[60] J. Kim and P. Moin, “Application of a fractional-step method to incompressible Navier-Stokes equations,” J. Comput. Phys. **59**, 308–323 (1985).
[61] S. Nagarajan, S. K. Lele, and J. H. Ferziger, “A robust high-order compact method for large eddy simulation,” J. Comput. Phys. **191**, 392–419 (2003).
[62] M. P. Simens, J. Jiménez, S. Hoyas, and Y. Mizuno, “A high-resolution code for turbulent boundary layers,” J. Comput. Phys. **228**, 4218–4231 (2009).
[63] G. Borrell, J. Sillero, and J. Jiménez, “A code for direct numerical simulation of turbulent boundary layers at high Reynolds numbers in BG/P supercomputers,” Comput. Fluid. **80**, 37–43 (2013).
[64] P. R. Spalart, R. D. Moser, and M. M. Rogers, “Spectral methods for the Navier-Stokes equations with one infinite and two periodic directions,” J. Comput. Phys. **96**, 297–324 (1991).
[65] D. J. C. Dennis and T. B. Nickels, “Experimental measurement of large-scale three-dimensional structures in a turbulent boundary layer. Part 1. Vortex packets,” J. Fluid Mech. **673**, 180–217 (2011).
[66] D. R. Cox and P. A. W. Lewis, *The Statistical Analysis of Series of Events* (Methuen & Co., 1966).
[67] A. Lozano-Durán and J. Jiménez, “Effect of the computational domain on direct simulations of turbulent channels up to $Re_\tau = 4200$,” Phys. Fluids **26**, 011702 (2014).
[68] J. P. Monty, N. Hutchins, H. C. H. Ng, I. Marusic, and M. S. Chong, “A comparison of turbulent pipe, channel and boundary layer flows,” J. Fluid Mech. **632**, 431–442 (2009).

[69] S. Hoyas and J. Jiménez, "Reynolds number effects on the Reynolds-stress budgets in turbulent channels," Phys. Fluids **20**, 101511 (2008).

[70] P. Bradshaw, "Inactive motions and pressure fluctuations in turbulent boundary layers," J. Fluid Mech. **30**, 241–258 (1967).

[71] C. D. Tomkins and R. J. Adrian, "Energetic spanwise modes in the logarithmic layer of a turbulent boundary layer," J. Fluid Mech. **545**, 141–162 (2005).

[72] C. R. Smith and S. P. Metzler, "The characteristics of low-speed streaks in the near-wall region of a turbulent boundary layer," J. Fluid Mech. **129**, 27–54 (1983).

[73] D. B. deGraaff and J. K. Eaton, "Reynolds number scaling of the flat-plate turbulent boundary layer," J. Fluid Mech. **422**, 319–346 (2000).

[74] M. Hultmark, M. Vallikivi, S. C. C. Bailey, and A. J. Smits, "Turbulent pipe flow at extreme Reynolds numbers," Phys. Rev. Lett. **108**, 094501 (2012).

[75] I. Marusic, J. P. Monty, M. Hultmark, and A. J. Smits, "On the logarithmic region in wall turbulence," J. Fluid Mech. **716**, R3 (2013).

[76] F. Harris, "On the use of windows for harmonic analysis with the discrete fourier transform," Proc. IEEE **66**, 51–83 (1978).

[77] P. D. Welch, "The use of fast Fourier transform for the estimation of power spectra: A method based on time averaging over short modified periodograms," IEEE Trans. Audio Electroacoust. **AU-15**, 70–73 (1967).

[78] G. K. Batchelor, *The Theory of Homogeneous Turbulence* (Cambridge University Press, 1953).

[79] P. L. O'Neill, D. Nicolaides, D. Honnery, and J. Soria, "Autocorrelation functions and the determination of integral length with reference to experimental and numerical data," in *Proceedings of the 15th Australasian Fluid Mechanics Conference: Sydney, Australia, 13-17 December* 2004, edited by M. Behnia, W. Lin, and G. D. McBain (The University of Sydney, 2004).

[80] T. Wei and W. W. Willmarth, "Reynolds-number effects on the structure of a turbulent channel flow," J. Fluid Mech. **204**, 57–95 (1989).

[81] J. Jiménez, "How linear is wall-bounded turbulence?" Phys. Fluids **25**, 110814 (2013).

[82] J. Jiménez, J. C. del Álamo, and O. Flores, "The large-scale dynamics of near-wall turbulence," J. Fluid Mech. **505**, 179–199 (2004).

[83] J. Jiménez and G. Kawahara, "Dynamics of wall-bounded turbulence," *Ten Chapters in Turbulence* (Cambridge University Press, 2013).

[84] N. N. Mansour, J. Kim, and P. Moin, "Reynolds-stress and dissipation-rate budgets in a turbulent channel flow," J. Fluid Mech. **194**, 15–44 (1988).

[85] J. M. Wallace, H. Eckelmann, and R. S. Brodkey, "The wall region in turbulent shear flow," J. Fluid Mech. **54**, 39–48 (1972).

[86] W. W. Willmarth and S. S. Lu, "Structure of the Reynolds stress near the wall," J. Fluid Mech. **55**, 65–92 (1972).

[87] R. A. Antonia, M. Teitel, J. Kim, and L. W. B. Browne, "Low-Reynolds-number effects in a fully developed turbulent channel flow," J. Fluid Mech. **236**, 579–605 (1992).

[88] C. J. Delo, R. M. Kelso, and A. J. Smits, "Three-dimensional structure of a low-Reynolds-number turbulent boundary layer," J. Fluid. Mech. **512**, 47–83 (2004).